Technical Report UILU-ENG 99-0515

AAE 99-15

FINAL TECHNICAL REPORT

For research supported by
AFOSR Contract No. F49620-97-J-0138

for period 2/15/97 to 12/15/98

Plasma Processes in Pulsed Plasma Microthrusters

prepared by

Rodney L. Burton(1),
M. J. Wilson(2), S. S. Bushman(2), and E. A. Antonsen(2)

Department of Aeronautical and Astronautical Engineering
University of Illinois at Urbana-Champaign
104 S. Wright Street
Urbana, IL 61801

Work supported by

Air Force Office of Scientific Research
Program Manager: Dr. Mitat Birkan

(1) Co-Principal Investigator; Dept. of Aeronautical and Astronautical Engineering
(2) Graduate Research Assistants; Ph.D. Candidates

September, 1999

Technical Report UILU-ENG 99-0515

AAE 99-15

FINAL TECHNICAL REPORT

For research supported by
AFOSR Contract No. F49620-97-J-0138

for period 2/15/97 to 12/15/98

Plasma Processes in Pulsed Plasma Microthrusters

prepared by

Rodney L. Burton(1),
M. J. Wilson(2), S. S. Bushman(2), and E. A. Antonsen(2)

Department of Aeronautical and Astronautical Engineering
University of Illinois at Urbana-Champaign
104 S. Wright Street
Urbana, IL 61801

Work supported by

Air Force Office of Scientific Research
Program Manager: Dr. Mitat Birkan

---

(1) Co-Principal Investigator; Dept. of Aeronautical and Astronautical Engineering
(2) Graduate Research Assistants; Ph.D. Candidates

September, 1999

REPORT DOCUMENTATION PAGE

Public reporting burden for this collection of information is estimated to average 1 hour per response, including tl
sources, gathering and maintaining the data needed and completing and reviewing the collection of information. ‹
aspect of the collection of information, including suggestions for reducing the burden to: Washington Headquarter
1216 Jefferson Davis highway, Suite 1204, Arlington, VA 22202-4302 and to the Office of Management and Bud
20503

AFRL-SR-BL-TR-99-
0303

1. AGENCY USE ONLY (Leave Blank)

2. REPORT DATE
Sept. 7, 1999

3. REPORT TYPE AND DATES COVERED
Final Report Feb. 15, 1997 - Dec. 15, 1998

4. TITLE AND SUBTITLE OF REPORT
Plasma Processes in Pulsed Plasma Microthrusters

5. FUNDING NUMBERS
AFOSR Contract No.
F49620-97-J-0138

6. AUTHOR(S)
Rodney L. Burton, M. J. Wilson, S. S. Bushman, and E. A. Antonsen

7. PERFORMING ORGANIZATION NAME(S) AND ADDRESS(ES)
University of Illinois at Urbana-Champaign
Dept. of Aeronautical and Astronautical Engineering
104 S. Wright St.
Urbana, IL 61801

8. PERFORMING ORGANIZATION REPORT NUMBER
AAE 99-15
Tech. Report UILU-ENG 99-0515

9. SPONSORING/MONITORING AGENCY NAME(S) AND ADDRESS(ES)
AFOSR/NA
801 North Randolph Road, Room 732
Arlington VA 22203-1977

10. SPONSORING/MONITORING ORGANIZATION REPORT NUMBER

11. SUPPLEMENTARY NOTES:

12a. DISTRIBUTION AVAILABILITY STATEMENT
Distribution Unlimited

12b. DISTRIBUTION CODE
Unlimited

13. ABSTRACT (Maximum 200 words)

This final technical report summarizes research on low-power pulsed Teflon™ plasma propulsion for satellites. Section I discusses a compact thrust stand used to make thrust and impulse bit measurements. Section II describes experimental measurements on a gasdynamic-type PPT in which measurements of magnetic field, electron number density, electron temperature, ion speed ratio and gas velocity are carried out by magnetic and advanced Langmuir probes. This section also describes thrust and heat-loss measurements. Section III outlines research with an electromagnetic-type PPT, intended to achieve very high specific impulse and efficiency.

14. SUBJECT TERMS
electric propulsion; plasma propulsion; thruster; pulsed plasma thruster; coaxial thruster

15. NUMBER OF PAGES:
65

16. PRICE CODE

17. SECURITY CLASSIFICATION OF REPORT: unclassified	18. SECURITY CLASSIFICATION OF THIS PAGE: unclassified	19. SECURITY CLASSIFICATION OF ABSTRACT: unclassified	20. LIMITATION OF ABSTRACT: unlimited

ONRCHI COMPUTER V1.0 11/94 STANDARD FORM 298 (REV 2-89)

Table of Contents

Abstract

This final technical report summarizes research on low-power pulsed Teflon™ plasma propulsion for satellites. Section I discusses a compact thrust stand used to make thrust and impulse bit measurements. Section II describes experimental measurements on a gasdynamic-type PPT in which measurements of magnetic field, electron number density, electron temperature, ion speed ratio and gas velocity are carried out by magnetic and advanced Langmuir probes. This section also describes thrust and heat-loss measurements. Section III outlines research with an electromagnetic-type PPT, intended to achieve very high specific impulse and efficiency.

Overview

Although the pulsed plasma thruster achieved flight status 35 years ago, a great deal of research needs to be performed to increase understanding of operational modes and increase performance. The approach at the University of Illinois is to emphasize an experimental approach, and to follow up later with numerical modeling.

The thrusters discussed here are all coaxial. This type of thruster has proven to generate high thrust at modest specific impulse (< 1000 s), and this type of performance is useful for Air Force missions where satellite aerodynamic drag is important. The thrusters are of two types. For the gasdynamic type, electrothermal heating and pressure dominate over electromagnetic $\vec{j} \times \vec{B}$ forces. For the electromagnetic type the reverse is true.

The first section of this report details with performance measurements. It was found that existing thrust stand designs required a large (2 m diameter) vacuum tank. Section I describes a smaller thrust stand suitable for a <1 m diameter vacuum tank. The complete description of this effort is not yet complete, and is waiting the M.S. thesis of M. J. Wilson. A copy of this thrust stand was fabricated for the Air Force Research Laboratory at Edwards AFB and is now in use there.

The second section of this report is based on the M.S. thesis of S. S. Bushman, and covers not only thruster performance of a gasdynamic-type PPT, but also detailed magnetic and electromagnetic surveys of the nozzle and plume. In addition, heat loss measurements are made to quantify this important area of thruster inefficiency.

The third section of this report is based on research by E. A. Antonsen, and covers initial the development of an electromagnetic-type PPT. As part of this effort SEM measurements are presented which shed light on the Teflon ablation process.

Work on this approach to the PPT is continuing. The coaxial PPT has been selected for the orbit transfer propulsion on the Air Force MightySat II.2 satellite, and a 100 W version is now being developed.

Section I.

Compact Thrust Stand for PPT Performance Measurements

Michael J. Wilson and Rodney L. Burton

An important experimental tool needed to evaluate the performance of the pulsed plasma thruster is a sensitive thrust stand. A compact, accurate stand was developed, calibrated and installed in the vacuum tank. The photograph below shows the stand with a coax PPT on the platform. The PPT is cable-driven, and the capacitor energy store (not shown) is located on the platform. This stand was discussed in a paper presented at the International Electric Propulsion Conference [Wilson, M. J., Bushman, S. S., and Burton, R. L., IEPC 97-122, Cleveland, 1997], and is the subject of an M.S. thesis.

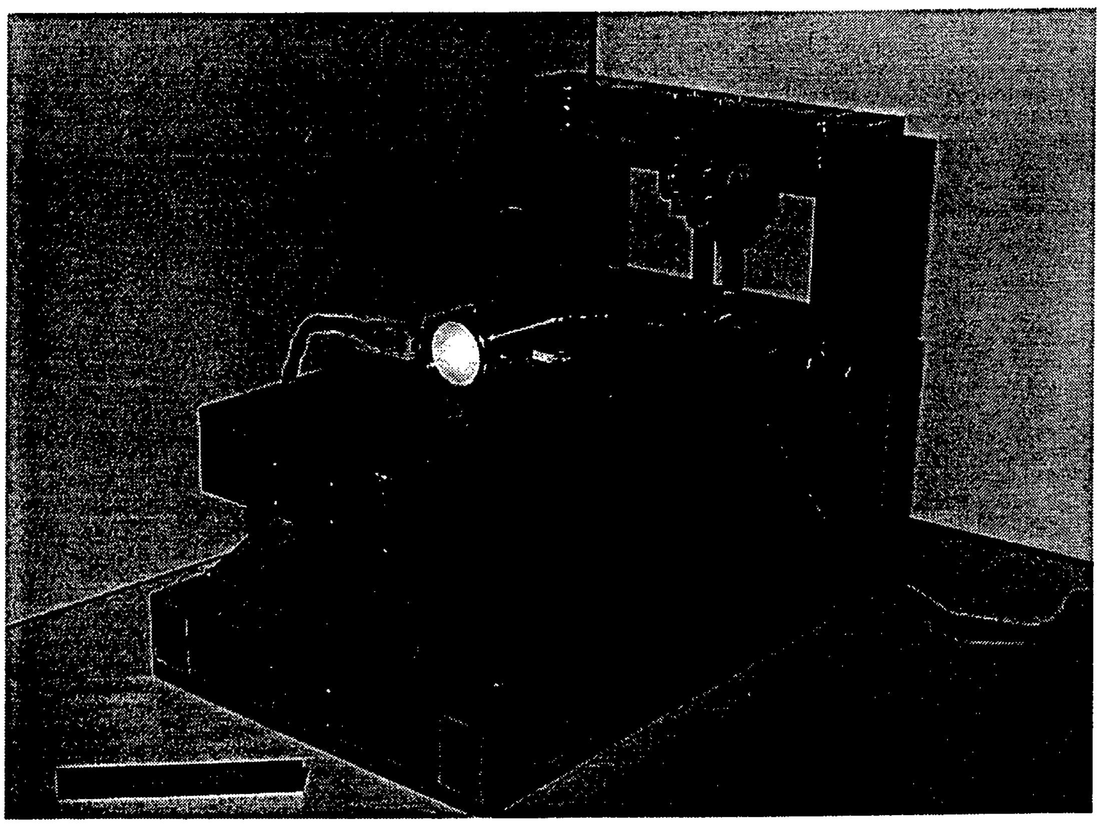

One of the difficult problems to solve with any thrust stand is thermal drift, as shown in the next figure. The lower trace shows the drifting displacement of the stand during calibration

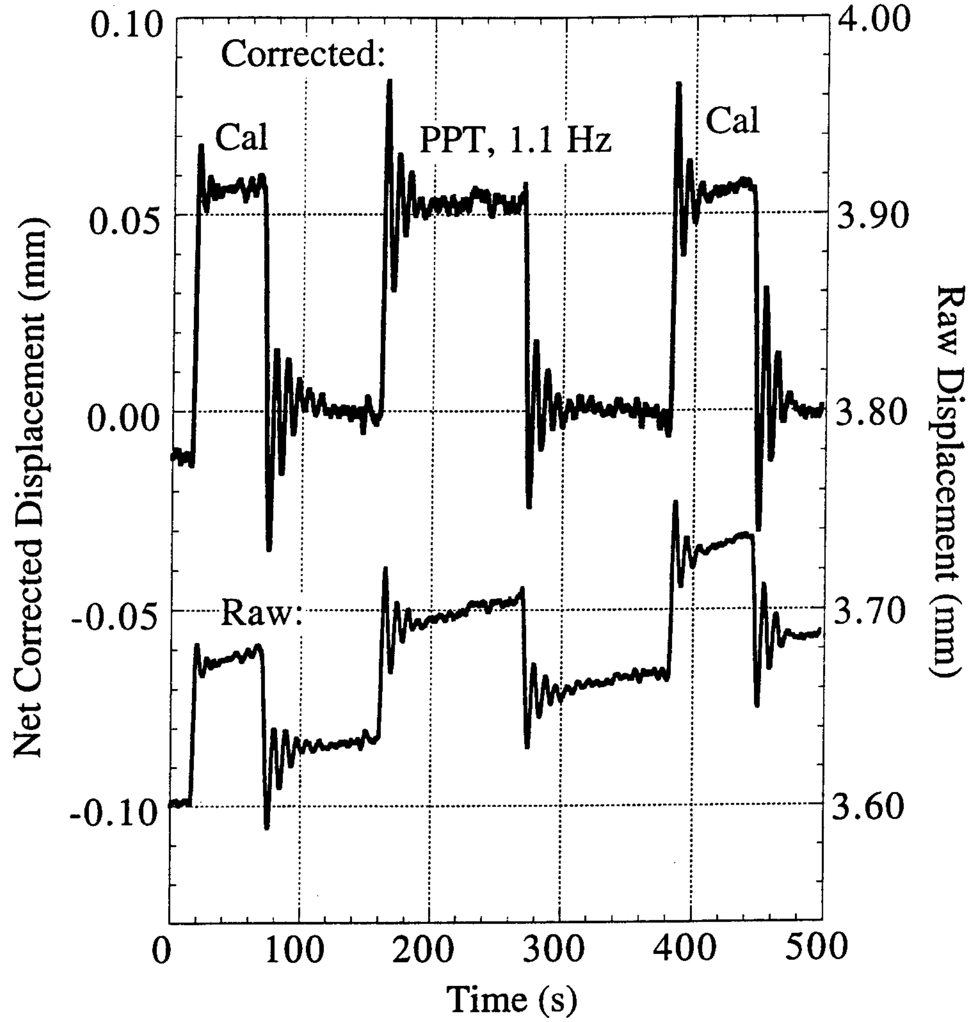

and repetitive operation. That the drift is constant in time can be seen by subtracting out an assumed constant drift (about 40 μm in 400 seconds) and replotting the results, as shown in the upper trace. The calibration weight used to produce the "Cal" signal is 300 μN, and the PPT thrust shown here is slightly less, about 280 μN.

The thrust stand can also be used to measure a single pulse, and the response to a calibration impulse is shown below. One of the most interesting aspects of the stand mechanism, which derives from Watt's "straight line motion" of 1784, is that extremely small yet repeatable vertical displacements can be achieved. Below, the stand is oscillating with a period of 10 seconds and a maximum displacement of 160 μm, producing a vertical displacement of the center of mass of $\Delta h \sim 10^{-10}$ m, the dimension of a hydrogen atom. This small displacement is a result of the small horizontal movement coupled with the large equivalent length of the long-period pendulum of nearly 100 m.

The stand was also calibrated by firing the same thruster on another stand at the Air Force Research Laboratory, Edwards AFB. The results are shown in the table. On an impulse bit basis

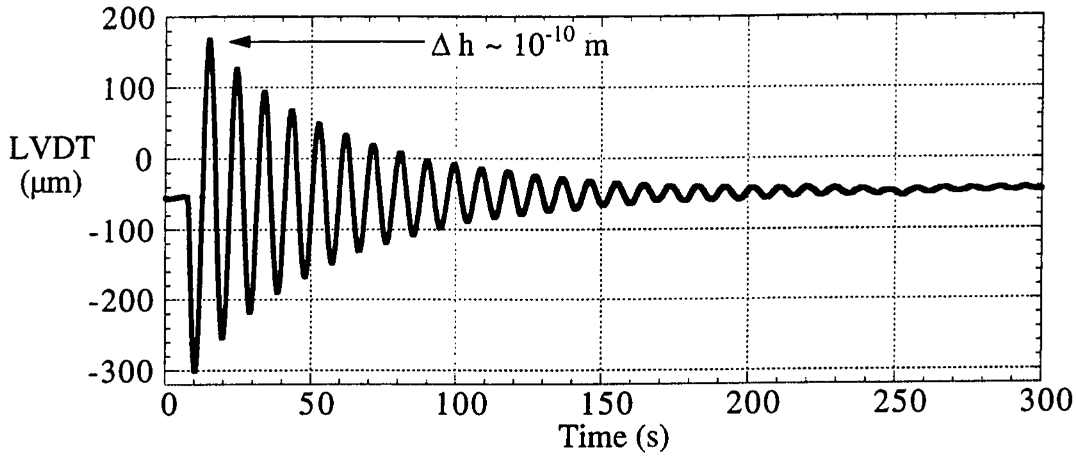

	Edwards AFRL	UIUC
E/Pulse, J	10	10
Freq., Hz	1.0	0.87
Δm/pulse, μg	36	36
Thrust, μN	187 ± 30	161 ± 8
I_{sp}, s	530 ± 85	524 ± 26
I_{bit}, μN-s	**187 ± 30**	**185 ± 9**

the agreement of I_{bit} is quite close.

The measured total impulse bit of the PPT over an energy range of 5 - 7.5 joules is shown in the next figure, compared to the LES-8/9 thruster. The impulse bit is approximately a constant 60 μN-s/joule over the measured range. This is 4 times the impulse bit of the LES-8/9. It is planned to extend the energy range in the near future to about 15 joules, for which the impulse bit is expected to continue to increase linearly. This is because both the electrothermal thrust, produced by pressure inside the thruster, and the electromagnetic factor $\int I^2 dt$ are proportional to the capacitor energy.

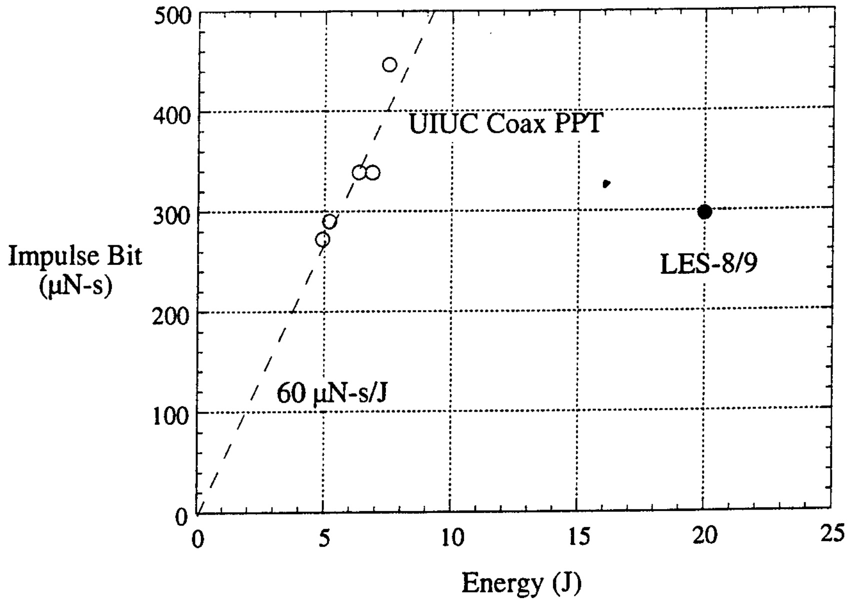

Knowing the mass loss Δm per pulse, the efficiency can be calculated, and is shown in the next figure. The efficiency is roughly double that of the LES-8/9, operating at higher energy. There are two reasons for this: better transfer of energy to the discharge, and better recovery of enthalpy in the PPT nozzle. The first factor is attributed to the non-reversing current, and the second partially due to the use of a fast pulse. It is expected that further improvements will lead to efficiencies above 20%, and perhaps 30%.

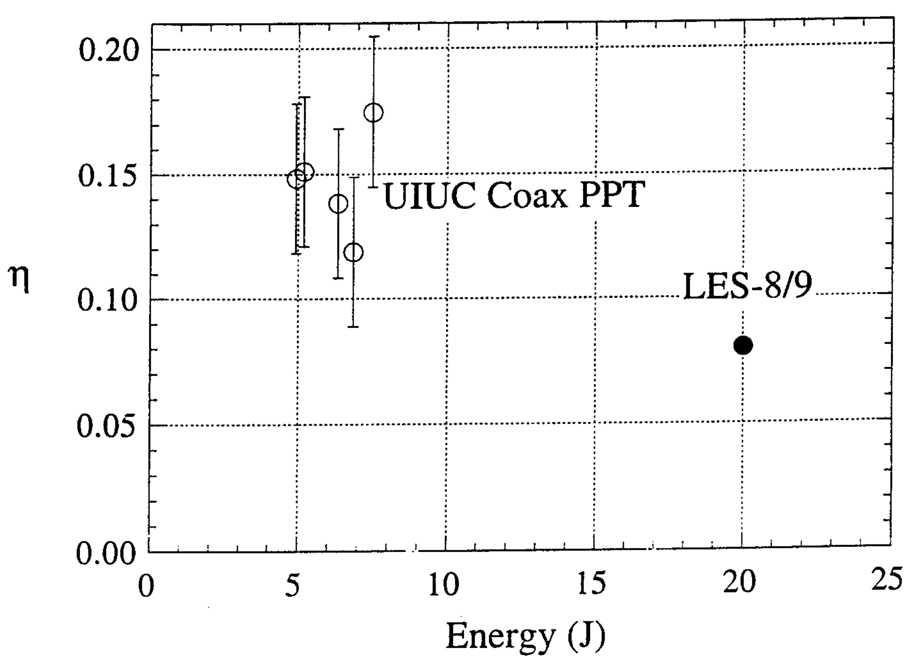

Section II.

Heating and Plasma Properties in a Coaxial Gasdynamic PPT

Stewart S. Bushman and Rodney L. Burton

Abstract

Multiple experimental diagnostics are used to characterize a coaxial pulsed plasma thruster, PPT–4. Operating at a capacitor stored energy E_o of 9 J, thermocouple data indicate that half of the energy that reaches the PPT is lost as heat to the walls. Thrust stand measurements yield an impulse bit of 29 ± 2 μN–s/J, corresponding to an I_{sp} of 745 ± 45 s and a thruster efficiency of 10.6 ± 1.3%. Quadruple electrostatic probe measurements indicate a symmetric plume with a peak electron density of $2.0 \pm 1.0 \cdot 10^{14}$ cm^{-3} and an initial electron temperature of 2.0 ± 0.3 eV. The ion mach number u_i/c_m is generally supersonic with a value of 3.0 ± 0.5. By measuring the arrival time of peak n_e, an ion velocity of 34 km/s is indicated. A magnetic probe survey indicates that the PPT–4 plume is not radially symmetric in B_θ. The radial plume asymmetry corresponds to a radial electromagnetic thrust component, calculated to be only 4% of the overall PPT thrust.

<u>Nomenclature</u>

A = probe surface area

A_{enc} = enclosed single B–probe coil area

B = magnetic field

c_m = most probable ion thermal speed

E_o = stored capacitor energy

k = Boltzmann's constant

I_{sp} = specific impulse

l_B = path length of constant B–field

Kn = Knudsen number

m = mass loss per PPT pulse

$\overline{m}_i$ = average ion mass

n = number of coils in B–probe

n_e = electron number density

n_i = ion number density

n_n = neutral number density

P_n = designation of probe n

$\dot{Q}$ = heating power

T_e = electron temperature

T_i = ion temperature

u_i = ion velocity

x_i = wake effect collection parameter

V_{d2} = P_1 and P_2 potential difference

V_{d3} = P_1 and P_3 potential difference

γ = ratio of specific heats

ε_o = permittivity constant

η_{dist} = distribution efficiency

η_{div} = divergence efficiency

η_f = frozen flow efficiency

η_h = heating efficiency

η_{loss} = heat loss efficiency

η_t = thruster efficiency

η_{tr} = transfer efficiency

λ_D = Debye length

λ_{a-b} = mean free path between a and b

λ_{mfp} = mean free path

μ_o = permeability constant

ϕ = e/kT_e, integrated B–probe signal

Introduction

The solid–propellant Pulsed Plasma Thruster (PPT) has a 35–year history of space operation, beginning in 1964 with the Soviet Zond–2 mission.[1,2] By providing a train of small, discrete impulse bits, PPTs are ideal for such diverse applications as orbit raising,[3] drag makeup,[4] attitude control,[5] constellation stationkeeping,[6] and deep–space missions.[7]

Teflon–fed PPTs are especially well–suited for low–thrust, on–board propulsion because they use a non–toxic propellant and are highly reliable, solid–state, low power, and lightweight, as they require no propellant storage system.[8] Additionally, as the thruster energy and pulse frequency are variable, PPTs are highly throttlable.

PPTs also have a history of low operational efficiency, generally calculated to be in the sub–10% range.[2] This characteristic of PPTs is largely due to both inefficient propellant utilization and poor energy efficiency due to transfer and thermal losses.[9] A primary goal of PPT research is to minimize these losses to make the thruster a more attractive option for future missions.

A schematic of a "traditional" rectangular, breech–fed PPT is depicted in Fig. 1. In PPT operation, the capacitor is charged to a prescribed energy, then the igniter plug fires. This results in electrical discharge across the face of the Teflon bar. Heat from the arc evaporates the Teflon, which is then accelerated electromagnetically and gas–dynamically out of the PPT nozzle. As the fuel is expended, more is advanced forward by a constant–force spring.[2]

Several characteristics of rectangular PPT operation complicate this process significantly. The geometry leads to edge effects, current gradients, and magnetic field asymmetry in the discharge.[10] Modeling this has proven especially difficult.[11] Igniter plug operation can result in shot–to–shot variation in PPT performance. The two acceleration mechan–isms are present in the PPT discharge, electrothermal (ET) and electromagnetic (EM), each interacting in wholly different ways with the plasma.[2] Despite the difficulties in deciphering exactly how the PPT operates, it is a proven, flight–qualified, and flight–tested technology.

Over the past three decades, several different PPT configurations have been investigated, exploring changes as minor as flared electrodes[12] to side–fed fuel bars[13] to a coaxial geometry[14] to combinations of these options: side–fed with flared electrodes[13] and coaxial geometry with side–fed bars.[15,16] This last, side–fed, coaxial configuration is the baseline PPT for the research presented here.[17] A schematic is provided in Fig. 2.

The operation for this coaxial geometry is similar to a rectangular PPT. A cavity is formed by the intersection of two Teflon bars held up against a central anode and two non–ablating boron nitride insulators. The anode is raised to a given potential by charging the capacitor. The igniter plug, mounted in a boron nitride nozzle, fires, resulting in an arc discharge between the anode and the annular cathode at the end of the nozzle. It is possible to modify PPT–4 to support four side–fed bars. Alternatively, a Teflon cylinder can be used in a "capillary" mode to simulate a 4–bar feed system.

In addition to the geometrical changes from the traditional PPT, the circuit has been modified. A diode has been installed across the terminals of the capacitors, preventing current reversal in the circuit and resulting in a unipolar current pulse. This current form is advantageous because it prevents a $\vec{j} \times \vec{B}$ field from accelerating propellant into the PPT, and it helps extend capacitor life by excluding it from the circuit after the first half–cycle.

These changes have resulted in a PPT performance regime that is primarily electrothermal. Arc heating from a ~10 J pulse produces a hot (1.5 eV), high–pressure (50 atm) plasma inside the cavity which is released as a rarefaction wave moves from the nozzle throat to the anode face. Experiments with the coaxial PPT geometry have resulted in the present iteration, PPT–4, shown in Figs. 2 and 3.

The cavity provides a small, enclosed volume where the vaporized Teflon is heated and pressurized by the arc and then expelled into a diverging nozzle, where it expands and accelerates, further increasing the exit velocity of the plasma. Because the current pulse is nonreversing, the net electromagnetic force, $\vec{F}_{EM} = \vec{j} \times \vec{B}$, is directed exclusively out of the PPT, maximizing that impulse component.

Experimental Apparatus

PPT–4 possesses an annular brass cathode with an inner diameter of 43 mm and a boron nitride (BN) nozzle with a 30° half–angle and an area ratio of 46:1. The igniter plug is a semiconductor–type aircraft combustor spark plug side–mounted in the nozzle. Teflon bars (25.4 mm long × 6.4 mm thick) are held firmly against the 4.8 mm diameter center anode by constant–force springs. Completing the cavity are two D–shaped pieces of BN. The center electrode (anode) is comprised of a 4.8 mm diameter threaded brass rod which can provide a variable cavity length.

Two diagnostics, a voltage probe and a Rogowski coil, are mounted in the back insulator. The thruster was designed to connect to a capacitive pulse–forming network (PFN) via a 2 cm long by 1 cm diameter coaxial steel and copper "stub" connector.

The PFN consists of four 2 μF oil–filled, high–voltage capacitors connected in parallel. Ring–down and PSpice[18] current matching yield an equivalent series resistance (ESR) of 7.5 mΩ and net inductance of 13 nH for the entire PFN. Two diodes have been placed across the terminals of each capacitor, resulting in zero PPT current reversal during the pulse. PSpice matching of the PPT current pulse at 9 J, displayed in Fig. 4, yields the external inductance L_{ext} = 82 nH and the arc impedance Z_{PPT} = 54 mΩ. The transmission line resistance is calculated to be 1 mΩ. The PPT–4 circuit schematic is shown in Fig. 5.

PPT–4 Life

New propellant bars inserted into the thruster undergo a "burn–in" phase whereupon the operation of the PPT reshapes the cavity into a steady–state shape which leaves a significant portion of the BN exposed to the arc, permitting loss of energy by heat transfer to nonablative material.

With a cylinder of Teflon used to yield a capillary mode of operation, the entire cavity is comprised of Teflon with no exposed insulation. However, additional fuel is not being fed into the system, so no steady–state shape arises. The cylinder simply "bores out" until the fuel is expended. Observations of this ablation indicate that it occurs evenly over the cylinder.

A typical PPT mission lifetime is required to be some 20 million pulses during on–orbit operation.[19] Of primary concern is whether or not the capacitors, the igniter plug, and the electrodes are capable of withstanding the rigors of constant firing for long periods of time. Capacitor life is shortened every time there is voltage on the terminals. By putting the diode in the PPT circuit, the capacitor voltage and current are zero after the first quarter–cycle, thus reducing the stress on the capacitor.

Circuit modeling (Fig. 6) indicates that voltage ringing is not totally eliminated in the capacitor, but the magnitude is reduced significantly. The voltage reversal with no diode is 33%, and with the diode is 13%. The stress on the capacitor is proportional to V^2, hence the imparted stress reversal for the diode case is six times less than if there is no diode installed. To further extend capacitor life, a diode can also be added in series with the capacitor to eliminate voltage reversal completely.

Metal erosion and carbon deposition are other processes which serve to reduce PPT life. PPT–4 has been fired successfully for ~70,000 shots with little evidence of ash accumulation on the plug. which is observed to have a clean tip. Minimal arc scoring is observed on the steel igniter plug exterior, but no discernible metal has been eroded.

Similarly, the brass electrodes have exhibited little evidence of metal erosion during the testing of PPT–4. Far more significant is the carbon deposition which completely blackens the exposed face of the central electrode and the chamfered part of the front electrode which completes the nozzle cone.

Thrust Mode

The electromagnetic and electrothermal thrust impulse of PPT–4 can be written as:

$$I_{bit} = \frac{1}{2} L'\Psi + I_{ET} \tag{1}$$

where L' is the inductance gradient, calculated from the PPT geometry and $\Psi = \int I^2\, dt$. For a coaxial thruster, assuming the current density is axisymmetric, L' is a function of the inner radius of the annular electrode r_a and the radius of the central electrode r_c:[2]

$$L'\ [\mathrm{H/m}] = \frac{\mu_o}{2\pi}\left[\ln\frac{r_a}{r_c} + \frac{3}{4}\right] \tag{2}$$

For PPT–4, $L' = 0.59$ μH/m. For the PPT–4 current pulse in Fig. 4, $\Psi = 115.1$ A–s. This predicts $I_{EM} = 4$ μN–s/J.

The electrothermal, or gasdynamic, contribution is dominated by the pressure force on the anode created by the ohmic heating of the ablated mass, roughly approximated by assuming that the stored energy E_o is delivered to the subsonic cavity, of volume $L_{cav} \times A_{cav}$, in an adiabatic, constant volume process, giving a pressure:

$$p_{cav} = \frac{(\gamma - 1)E_{cav}}{A_{cav}L_{cav}} \tag{3}$$

The gasdynamic impulse bit per Joule is then:

$$\frac{I_{ET}}{E_o} \approx \frac{(\gamma - 1)}{a}\frac{E_{cav}}{E_o} \tag{4}$$

At an estimated plasma temperature of 1.5 eV, $\gamma = 1.3$, sound speed $a = 4.5$ km/s from the SESAME code results for Teflon,[20] and, assuming 50% of E_o is lost as heat to the wall, $E_{cav}/E_o = 0.5$ giving $I_{ET} = 33$ μN–s/J. This estimate is higher than the measured I_{ET} by 30%. Clearly, PPT–4 is dominated by the gasdynamic impulse component which by this estimate comprises 89% of the total impulse bit.

Plasma Diagnostics

The PPT exhausts into a 1 m diameter × 1.5 m long vacuum tank, held at vacuum by a 1500 l/s turbomolecular pump which provides a typical operating environment of 30 μTorr. Two types of plasma probes were used in this research: a quadruple electrostatic probe and a magnetic probe. The probes were mounted on a linear translation carriage developed by Bufton.

The PPT centerline is defined as the z–axis in cylindrical coordinates. Positive z are measured from the downstream face of the annular electrode (cathode). Radial distance from centerline is denoted by r, and θ is measured from the spark plug location, which corresponds to $\theta = 0$.

The quadruple probe used here, derived from a previous design,[21] consists of three 0.3 mm–diameter by 2.3 mm–long cylindrical tungsten probes (P_1, P_2, and P_3) which are aligned parallel to the flow velocity and one 0.3 mm–diameter by 2.5 mm–long tungsten probe (P_4) which is perpendicular to the flow. The probes are mounted in a round, quad–bore, insulating alumina ($Al_2 0_3$) tube (3.2 mm o.d. x 0.5 mm i.d.). A quadruple probe schematic is in Fig. 7.

The detailed magnetic field strength distribution in the nozzle and plume of PPT–4 is measured with a magnetic probe (B–probe),[22] pictured in Fig. 8, consisting of 4 turns of 30–gauge magnet wire shielded in Pyrex. The wire leads are tightly twisted to minimize extraneous field collection area and fed through single–bore alumina tubing into a thermocouple fitting identical to that of the quadruple probe. Integrating the raw B–probe voltage signal ($V = d\phi/dt$) gives B_θ.

The enclosed current I_{enc} is evaluated approximately from:

$$I_{enc} = \frac{B_\theta l_B}{\mu_o} = \frac{\phi l_B}{\mu_o n A_{enc}} \qquad (5)$$

where l_B is a nearly–circular path length of constant magnetic field.

Quadruple Probe Theory

The quadruple probe circuit is depicted in Fig. 9. The electrically floating probe, P_2, assumes the floating potential V_f of the plasma. P_3 and P_4 are biased at $V_{d3} = V_{d4} = 12$ volts negative with respect to P_1 to collect saturation ion currents I_3 and I_4. The probe output consists of the potential of the floating probe V_{d2} relative to P_1 and the time–dependent ion current histories to the biased probes.

Quadruple probe theory is well documented[21,23] and will not be repeated here. This theory is based on operating in a collisionless regime with a thin ion sheath and a Maxwellian electron energy distribution, with corrections made for near–probe collisions.[17]

For a quadruple probe with electrode surface areas $A_1 = A_2 = A_3$ and electrode biasing such that $V_{d3} = V_{d4}$, the electron temperature T_e [eV] $= 1/\phi$ is calculated from:

$$1 = \frac{1 + \exp(\phi V_{d3}) - 2\exp[\phi(V_{d3} - V_{d2})]}{(I_4/I_3)\{\exp[\phi(V_{d3} - V_{d2})] - 1\}} \tag{6}$$

Solved iteratively, (6) uniquely determines electron temperature as a function of measured quantities V_{d2} and I_4/I_3 and known V_{d2}. The electron density, n_e, is calculated for a neutral Teflon plasma ($n_e = n_{C^+} + n_{F^+}$):

$$n_e = \frac{\frac{\kappa}{\beta}\left(\frac{I_3}{A_3}\right)\left(1 + \frac{I_4}{I_3}\right)\exp\left(\frac{1}{2}\right)\left(\overline{m}_i\right)^{1/2}}{e\left(kT_e\right)^{1/2}\left[\exp(\phi V_{d2}) - 1\right]} \tag{7}$$

where $\overline{m}_i = 16.7$ amu is the average ion mass, $\beta = (\overline{m}_i/m_{C^+})^{1/2} = 1.18$ and κ is an electron density correction to account for multiple ion species:

$$\kappa = \frac{1 + \left(\frac{n_{F^+}}{n_{C^+}}\right)}{1 + \left(\frac{n_{F^+}}{n_{C^+}}\right)\left(\frac{m_{C^+}}{m_{F^+}}\right)^{1/2}} \tag{8}$$

The number density ratio is roughly equal to the inverse ratio of ionization potentials:

$$\frac{n_{F^+}}{n_{C^+}} \approx \frac{2\varepsilon_{i_C}}{\varepsilon_{i_F}} = \frac{2 \times 11.3}{17.4} = 1.3$$

yielding a value for $\kappa = 1.13$, a value which nearly cancels the mass correction factor β of 1.18.

The crossed electrostatic probe incorporated into the quadruple probe by way of the perpendicular electrode P_4 provides the ion speed ratio, or Mach number, u_i/c_m, where u_i is the ion directed velocity and $c_m = (2kT_i/\overline{m}_i)^{1/2}$ is the most probable thermal speed of the collected ions. For the case of two equally biased collisionless probes, one probe parallel to the flow axis and one normal, as P_3 and P_4 are, respectively, the single–species collected ion current ratio for the thin sheath case I_4/I_3 is used to determine u_i/c_m.

The plasma flowing over the perpendicular electrode induces a wake which prevents a fraction of A_4 from collecting ions. The wake is accounted for by x_i, the geometric fraction of A_4 available for ion collection. The extent of the wake effect is determined by an estimate of the u_i/c_m relation. If $u_i/c_m \geq 2$, the flow is "hypersonic," and only the projected area of A_4 is available for ion collection; hence $x_i = 1/\pi$. If u_i/c_m is of the order of 1, the effect is less pronounced, and the entire front half of the electrode is available such that $x_i = 1/2$. If the plasma were stationary, then there would be no correction ($x_i = 1$).[21,23] Curves of u_i/c_m as a function of I_4/I_3 are plotted in Fig. 10 for three cases of x_i.

For the high–pressure, high–temperature plasma in the cavity of a coaxial PPT, $T_i \approx T_e \approx 1.5$ eV. For $u_i \approx 10$ km/s, $c_m = 4.2$ km/s and $u_i/c_m = 2.1$. Therefore for this investigation, $x_i = 1/\pi$.

Probe Measurement Uncertainty

Uncertainty in the quadruple probe measurements of n_e, T_e, and u_i/c_m stems from experimental error in measured quantities as well as systematic error inherent in the probe environment and the quadruple probe theory and its assumptions.

The experimental error in the quadruple probe data corresponds to measurement uncertainties in the probe current, voltage, and geometries. These yield RMS experimental uncertainties for n_e (± 7%), T_e (± 10%), and u_i/c_m (± 11%).

Evaluating systematic uncertainties requires evaluation of several plasma length scales. Quasineutrality is assumed. For the conditions at the exit plane of PPT–4 of $n_e = 5 \cdot 10^{14}$ cm^{-3}, $n_n = 10^{16}$ cm^{-3}, and $T_e = 1.5$ eV), the Debye length λ_D is $4.1 \cdot 10^{-5}$ cm. The tungsten electrodes have a radius r_p of 0.016 cm. The probe radius/Debye length ratio r_p/λ_D is ≈ 400, establishing that the thin sheath assumption is satisfied and that there are no sheath interactions in between probe electrodes.

Charged particle mean free paths λ_{e-e}, λ_{e-i}, λ_{i-i} are estimated as 355 times the Debye length. For ion–neutral and neutral–neutral collisions, the corresponding mean free paths λ_{i-n} and λ_{n-n} are 2500 times the Debye length.

Charged particle collisions which serve to affect the collected current must also be considered. The Knudsen numbers (λ_{mfp}/r_p) for electron and ion collisions based on probe radius are ≈ 1, the transition regime where collected current is affected by collisions. While the effect of charged particle collisions on electrostatic probe response for $Kn_{e-e} = Kn_{e-i} = Kn_{i-i} \approx 1$ has been largely unexamined, some work has been done to attempt to quantify the systematic error these conditions will impart on the probe current.[24,25] Generally, results suggest that the ion–neutral Knudsen number Kn_{i-n} determines how the probe will respond to charged particle collisions.

For $Kn_{i-n} \leq 1$, the ion current decreases with respect to the collisionless case, and for $Kn_{i-n} >> 1$, the ion current increases.[24] Under the established plasma conditions, $Kn_{i-n} = 63 >> 1$, resulting in increased ion current. Tilley et al. conclude that collisions in the charged particle transitional regime with a high Kn_{i-n} produce an increase in ion current of about 10–20%.[25]

The increase in ion current will correspond to a 10–20% increase in calculated n_e because n_e is directly proportional to I_3. However because both I_3 and I_4 are ion attractors, the ratio I_4/I_3 should remain relatively unchanged, leading to a negligible change in T_e and u_i/c_m, which are both solely functions of I_4/I_3.

When the "end effect parameter" $\tau_L = (L_p/\lambda_d)(kT_e/\overline{m}_i)^{1/2}/u_i$ is greater than 50, a cylindrical probe in a flowing plasma will not be sensitive to small–angle misalignments between the electrode and the flow axis.[24] For $u_i \approx 10$ km/s, $\tau_L = 1663$, satisfying the > 50 condition. In addition, the probe tip collects convected charged particles. From the probe geometry and assumed conditions ($u_i \approx 10$ km/s, $n_i = 5 \cdot 10^{14}$ cm^{-3}), there is an estimated overstatement of n_e of 12%,[17] while this effect has no significant impact on T_e or u_i/c_m.

From the established uncertainty for n_e, a correction factor C = 0.78 is employed to account for charged particle collisions and collected tip current. Triple probe model assumptions, including the Bohm sheath model and the thin sheath approximation, impart an additional uncertainty of ± 50% on the n_e calculation. Theoretical assumptions additionally place an uncertainty of ± 10% on the T_e calculation.[25] The total RMS uncertainties for n_e, T_e, and u_i/c_m are thus 51%, 14%, and 15%, respectively.

Experimental Results

To increase performance, the PPT was run in the capillary mode, with cavity length 8.3 mm, diameter 4.8 mm, and pulse length to acoustic time ratio $t_p/t_a \approx 4$. The baseline conditions are 9 J at 1500 V and 1.1 pulses per second, giving 10 W. Additional tests were taken 5 and 15 J at 1.1 PPS.

Heat Measurements

The coaxial geometry of PPT–4 permits approximate measurement of wall heating losses. The PPT–4 thruster head is separated from the capacitor bank by a coaxial stub connector. Thermal losses are determined by measuring the temperature rise rate dT/dt seen by thermocouples fastened to the outside of the aluminum thruster body, the stub connector, and the capacitors.

To quantify the effect of propellant geometry and type on thermal losses, three configurations are used. The thruster is operated in 2–bar and capillary mode with standard Teflon. Additionally, commercial extruded Teflon tubing, which is translucent rather than the opaque white of virgin Teflon, was used in capillary mode after preliminary tests suggested that radiation through the translucent wall would result in greater thermal losses.

The thermal mass of the thruster head is determined from an inventory of component masses and specific heats. For the thruster head, $\Sigma mc_p = 462$ J/°K. For the stub connector, $\Sigma mc_p = 38$ J/°K.

The heating rate data was corrected for the axial heat flow along the stainless steel stub connector. The stub heat flow is $\dot{Q}_{stub}$ [W] $= kA_{stub}\Delta T/L_{stub}$ where $kA_{stub}/L_{stub} = 0.036$ W/°K.

Measurements were taken at energies $E_o = 5$, 9, and 15 J in both 2–bar and capillary mode configurations. With the thruster pulsing at 1.1 PPS, the temperature rise rate increases slowly and becomes linear (constant dT/dt) after about 100 seconds. All thermocouple tests performed were for 1000 shots, with additional data taken after the PPT stopped firing until the temperature rise leveled off. Temperature rate measurements were accurate to ± 0.015 °K/min.

The temperature rise rate is combined with the thermal mass, the heat loss through the stub connector, and a cavity radiative loss to yield the total heating loss, $\dot{Q}_{PPT}$. The mean radiative power loss $\dot{Q}_{rad}$ out of the front of the PPT–4 cavity is estimated as 0.4 J/pulse, assuming a 1.5 eV blackbody and a 4 μs pulse.

The heat loss efficiency η_{loss}, which is the fraction of the energy delivered to the thruster head available for accelerating propellant is then:

$$\eta_{loss} = \frac{\dot{Q}_{PPT}}{P_{term}} \qquad (9)$$

where the terminal power P_{term} is the power transferred to the thruster head from the PFN.

Internal capacitor heating is expressed in terms of a capacitor–to–arc transfer efficiency η_{tr}. A heat rise of 0.03 ± 0.01 °K/min is measured in the capacitors for the 9 J case, and the thermal mass is estimated to be 2100 J/°K, giving 1.1 W in capacitor heating and $\eta_{tr} = 0.89$.

The heating power, terminal power, and heating efficiency are listed in Table 1 for the various configurations and energies.

Table 1: PPT–4 Thermal Power Losses

Configuration	E_0 [J]	$\dot{Q}_{PPT}$ [W]	P_{term} [W]	η_{loss}
2–Bar	5	3.6	4.9	73%
	9	5.7	8.8	65%
	15	9.3	14.6	64%
Capillary				
White	5	2.9	4.9	59%
	9	4.5	8.8	51%
	15	5.5	14.6	37%
Translucent	9	4.8	8.8	55%

As expected, losses are highest for the 2–bar configurations and the least for the capillary geometries. This is due to the insulator exposure of 33% of the cavity circumference in the 2–bar mode, compared to zero exposure in capillary mode. The most significant result is that 37 – 73% of the input power is lost as heat for all configurations tested. The translucent capillary, as anticipated, was less efficient than the opaque Teflon under the same operating conditions. The most efficient configuration is the 15 J capillary case with the lowest thermal loss (5.4 W out of 14.6 W). This implies that the PPT may run more efficiently at higher energies.

Thrust and Thruster Efficiency

The performance of PPT–4 was measured to within ±6% at 9 J on the UIUC Compact Thrust Stand,[16] using a single–pulse method. Neglecting one shot which was 20% higher than the others, a conservative average impulse bit for the remaining pulses is $I_{bit} = 260 \pm 16$ μN–s. This result also can be expressed as $I_{bit}/E_o = 29 \pm 2$ μN–s/J, approximately twice the level achieved by the LES–8/9 PPT operating at 20 J.[2]

Mass loss measurements indicate a decline in mass loss per pulse per unit energy over time. The results, plotted in Fig. 11, indicate a range of ablation rates. Using an average value of $\Delta m/E_o$ gives a thruster efficiency $\eta_t = 10.6 \pm 1.3\%$ at 9 J. The I_{sp} is 745 ± 45 s.

Efficiency Analysis

The thruster efficiency η_t can be written as the product of component efficiencies during thruster operation:[26]

$$\eta_t = \eta_{tr} \times \eta_h \times \eta_f \times \eta_{div} \times \eta_{dist} \tag{10}$$

where η_{tr} is the transfer efficiency, η_h is the heating efficiency $1-\eta_{loss}$, η_f is the frozen flow efficiency, η_{div} is the flow divergence efficiency, and η_{dist} is the flow distribution efficiency. For operation in capillary mode at $E_o = 9$ J, $\eta_{tr} = 0.89$ and $\eta_h = 0.49$.

The frozen flow efficiency $\eta_f = u^2/2h_o$ is estimated from:

$$h_o = \frac{5}{2}T + \left(\varepsilon_i\right)_z + \frac{1}{2}u^2 \text{ [eV]} \tag{11}$$

where Z = charge state and all quantities are in electron volts. The frozen flow efficiency is dominated by the low–speed neutral particles, so that $(\varepsilon_i)_z$ is negligible. The ion temperature in the exhaust flow is expected to be lower in the diverging nozzle than in the cavity. Using the Spitzer resistivity relation[27] with the modeled PPT impedance ($Z_{PPT} = 54$ mΩ), the cavity temperature is estimated to be 1.5 eV, and the ion temperature in the nozzle is assumed to be ~

1.0 eV. Based on the PPT–4 mass–averaged exhaust velocity 7.3 km/s, the frozen flow efficiency is estimated to be $\eta_f \approx 0.65$.

The divergence efficiency results from radial momentum created by the 30° half–angle nozzle,[28] and is estimated as $\eta_{div} \approx 0.93$.

The distribution efficiency η_{dist} quantifies velocity profile losses in the thruster, including effects such as velocity loss caused by viscous drag at the walls. Consequently, it requires a detailed knowledge of the flow velocity distribution in PPT–4. This measurement has not yet been performed on any PPT, but since η_t is known (using an average $\eta_t = 11\%$), and the other four efficiencies have been measured, estimated, or calculated:

$$\eta_t = \eta_{tr} \times \eta_h \times \eta_f \times \eta_{div} \times \eta_{dist}$$

$$.11 = .89 \times .49 \times .65 \times .93 \times \eta_{dist}$$

This yields the distribution efficiency $\eta_{dist} = 0.42$. This efficiency represents a loss of thrust due to the slow neutrals. A detailed energy balance is presented??in Table 2 .

Table SEQ Table * ARABIC 2 : PPT–4 Energy Balance at Eo = 9 J

Type	Efficiency	Loss [J]
η_{tr}	.89	0.99
η_h	.49	4.09
η_f	.65	1.37
η_{div}	.93	0.18
η_{dist}	.42	1.38
η_t	.11	8.01

Quadruple Probe Measurements

The quadruple probe was employed to measure electron density n_e, electron temperature T_e, and ion Mach number u_i/c_m outside the nozzle in the near– and far–field exhaust plume. Attempts were made to probe inside the nozzle, but a change in the shape of the current pulse was observed, suggesting that the current may have been arcing to the probe electrodes.

Measurements were made from $z = 0$ (the exit plane) to $z = +18$ cm along the PPT centerline axis at $E_0 = 9$ J. Off–centerline, or "off–axis," measurements were taken by both translating and rotating the probe on the carriage such that the probe was aligned with the plasma flow vector. All probing locations are shown in Fig. 12.

A high–frequency noise signal (~1.4 MHz) was present for all measured probe data which was of a particularly large amplitude during the current pulse, so that data taken during the first 8 μs following ignition was unusable. To reduce noise, a moving–average smoothing routine was applied to a 10–shot average data signal. Sample smoothed probe output is depicted in Fig. 13.

It was also discovered that after ~50 shots, a layer of accumulated Teflon ash deposited on the probes, resulting in a 5–10% decrease in I_3 and I_4. To avoid this problem, the probes were cleaned using ion bombardment before all tests began and following every 30 firings thereafter. The probes were each raised to a potential of 1 kV, and then the chamber was briefly flooded with air through a port directly below the quadruple probe. Once the tank pressure dropped to the Paschen breakdown limit, the electrodes underwent a glow discharge. This discharge was maintained for only a few seconds, as longer durations resulted in melting the tungsten wire. Once the cleaning technique was employed, no significant decrease in I_3 or I_4 was discernible under similar operating conditions.

A typical reduced quadruple probe data set is presented in Fig. 14. The case shown corresponds to centerline data at $z = 3.0$ cm and $E_0 = 9$ J. Electron density n_e experiences an initial rise, peaking at $2.0 \pm 1.0 \cdot 10^{14}$ cm^{-3} at 14 μs, followed by a slow decay. Electron temperature T_e starts at 2.0 ± 0.3 eV at 8 μs, and then slowly cools to about 0.33 ± 0.05 eV at late times. Ion Mach number u_i/c_m maintains a relatively constant supersonic value of 3.0 ± 0.5. While the magnitudes and peak times do vary for other cases, the shapes of the curves are relatively consistent for all locations and energies.

Peak centerline values of n_e and the times of peak n_e for $E_0 = 9$ J are plotted in Fig. 15 versus distance from the exit plane. A straight–line fit of the n_e peak times from $z = 5$ to $z = 18$ suggests an electron/ion velocity of 34 km/s, a value well–supported by measurements in rectangular

PPTs.[2] A curve fit of the electron density data indicates a peak in n_e occurring at $z \approx 4$ cm. Near–field data for $E_o = 5$ and 15 J, while insufficient to establish a velocity, indicate a negligible change in n_e for all cases ($n_e \sim 2 \cdot 10^{14}$ cm^{-3}).

Centerline electron temperature varies very little for the measured probe locations. At E_o of both 9 and 15 J, T_e starts at 2.0 ± 0.3 eV and then steadily decreases to about 0.4 ± 0.06 eV. At $E_o = 5$ J, T_e typically starts at 1.0 ± 0.2 eV, and drops to 0.4 ± 0.06 eV.

Centerline ion Mach number, similarly, is relatively constant at a supersonic value of 3.0 ± 0.5 with two exceptions. In the far field at $E_o = 9$ J, u_i/c_m jumps to a hypersonic value of 7.5 ± 1.1. Additionally, at $E_o = 5$ J, u_i/c_m reaches as high as 5.0 ± 0.8. In both cases, the ions are still at high velocities, suggesting a colder plasma, resulting in a higher Mach number.

Off–axis n_e results at $E_o = 9$ J, $z = 1.3$ cm, and $r = 2.1$ cm, depicted in Fig. 16, demonstrate remarkable symmetry in the plume at varying values of θ. The measured peak $n_e = 1.0 \pm 0.5 \cdot 10^{14}$ cm^{-3} is considerably lower than the corresponding interpolated peak value on centerline from Fig. 15 of $n_e = 1.3 \pm 0.7 \cdot 10^{14}$ cm^{-3}. Further out in the plume at $z = 3.0$ cm and $r = 2.8$ cm, the electron density drops to $0.8 \pm 0.4 \cdot 10^{14}$ cm^{-3}, compared with a centerline value of $n_e = 2.0 \pm 1.0 \cdot 10^{14}$ cm^{-3}. These data suggest a decreasing density distribution across the exit plane and further out into the plasma.

Also interesting are the off–axis T_e results. The data indicate that the off–axis plasma at $T_e = 1.5 \pm 0.2$ eV is considerably hotter than the centerline plasma ($T_e \sim 0.4$ eV) for the entire 30 μs of data acquisition. At the same time, off–axis ion Mach number data exhibit little variation from the centerline values, remaining relatively constant at a supersonic value of 2.5 ± 0.4 at all probed off–axis locations. It is possible that the off–axis flow is non–equilibrium, as has been found for arcjets.[29]

Ion Mach Number and Velocity

A maximum c_m is calculated by assuming thermal equilibrium: $T_e = T_i \approx 1.5$ eV. This results in $c_m = (2kT_i/\overline{m}_i)^{1/2} = 4.2$ km/s, a value nearly equal to the sound speed for a 1.5 eV Teflon vapor determined by the SESAME code.[20] Centerline and off–axis ion Mach numbers ranging from 2.5 to 7.5 indicate that the ions are traveling from 11 to 32 km/s, values in agreement with published data[2] for rectangular PPTs as well as with the 34 km/s value measured in Fig. 15.

The measured specific impulse I_{sp} = 745 s gives a mass–averaged exhaust velocity u_e = 7.3 km/s, nearly twice c_m, implying that the nozzle is effectively accelerating the exhaust mass. If late–time ablation, which exhausts heavy Teflon particulates at very low velocities (≤ 0.2 km/s),[9] is taken into consideration, u_e is skewed even higher. The high values of u_i/c_m are encouraging for the continuing development of higher–efficiency PPTs.

Magnetic Probe Measurements

A four turn, 0.94 mm diameter magnetic probe was used to measure magnetic field strength and identify enclosed current I_{enc} contours inside the nozzle and in the near–field exhaust plume. Probing proceeded in the nozzle to z = –25 mm, where the ratio of the nozzle diameter to the Pyrex probe sheath diameter was ~10:1.

The 99 probing locations in the θ = 0°–180° plane are plotted in Fig. 17. Data was taken along four equally–spaced planes, with the 0° plane defined as that containing the igniter plug. All magnetic field data were taken at E_o = 9 J and recorded as an average of 30 PPT firings at each probe location.

A probe calibration yielded nA_{enc} 5% over the geometric value. Uncertainty in data due to shot–to–shot variation is ±12% at low values of B_θ (~30 mT), dropping to 4% for $150 \le B_\theta \le 300$ mT.

The most significant conclusion drawn from the magnetic field data is that the PPT–4 plume is not azimuthally symmetric in B_θ, as depicted in Fig. 18, which shows B_θ signals with the Pyrex sheath in contact with the nozzle wall at r = 8.1 mm. The smaller signal, peaking at B_θ = 150 ± 6 mT occurs at θ = 0°, corresponding to the location of the spark plug. The maximum signal, peaking at B_θ = 323 ± 13 mT, occurs at θ = 180°, directly opposite from the plug. The 180° signal falls to zero at 4 μs, well before the end of the current pulse.

The contour plot in Fig. 19 is the nozzle cross–section at z = –24 mm and t = 2.5 μs, corresponding to a near–peak current of 8.0 kA. The spark plug position in (r,θ) is as indicated, although it is centered at z = –19.1 mm, 5 mm forward of the contour plot. Curves of constant enclosed current are designated, as is total enclosed current I_{tot} = 8.0 kA. The contours clearly indicate the lack of current symmetry in the system. Data taken further out in the plume indicate that peak magnetic field decreases to ~150 mT at z = –15 and to ~50 mT at z = 0.

The side–view contour plot pictured in Fig. 20, which occurs at the same time as Fig. 19, indicate a reflected symmetry about the 90° – 270° plane inside the nozzle of PPT–4. Additional data taken during the pulse show that the 90°–270° plane symmetry initiates by t = 1.5 μs and dissipates by t = 4.0 μs, although the total current has decreased to 2.4 kA by this time. There is never any observed symmetry in 0°–180° plane contours; however the discussed magnetic field asymmetry deep inside the nozzle is clearly visible.

As discussed earlier, PPT–4 possesses an estimated electromagnetic thrust component of 36 μN–s at E_o = 9 J. PPT–4's thrust is dominated by the electrothermal impulse bit, which generates the remaining 86% of the thrust (I_{ET} = 224 μN–s). The high degree of symmetry in the quadruple probe measurements indicates that the electrothermal component expands normally about the centerline with no radial electrothermal thrust component.

Even if the electromagnetic thrust vector is off–axis as much as 15%, a value not wholly unreasonable considering Fig. 19, the peak radial thrust is 9 μN–s, only 3.5% of the overall thrust.

Hall Parameter and Plasma Conductivity

The data obtained by the magnetic and quadruple probe can be used to calculate the Hall parameter Ω.[1] At the exit plane, $n_e = 1.1 \cdot 10^{14}$ cm^{-3} and $n_n \approx 10^{16}$ cm^{-3}. Assuming a constant mass flow rate at a constant exhaust velocity, the estimated nozzle throat densities are $n_e \approx 1.0 \cdot 10^{16}$ cm^{-3} and $n_n \approx 10^{18}$ cm^{-3}. The electron temperature at the exit plane is $T_e \approx 1.5$ eV. At the specified plasma conditions, the plasma conductivity σ_o = 1850 (Ω–m)$^{-1}$. At a maximum measured magnetic field of 323 mT, the Hall parameter $\Omega = 0.4$. This result is relatively insensitive to increases in electron temperature, which may occur in and near the cavity. The Hall parameter remains near 0.4 for $1.3 \leq T_e \leq 6$ eV, so that plasma conductivity is somewhat reduced by the crossed electric and magnetic fields.

Conclusion

Using a variety of diagnostics, including thermocouples, a thrust stand, a quadruple electrostatic probe, and a magnetic probe, the performance of a coaxial PPT operating in a capillary mode is measured and its plume is explored. Established quadruple probe theory has been modified for the Teflon plasma, and corrections and uncertainties specific to the exhaust density and temperature have been calculated.

Thermocouples on the thruster, the stub connector, and the capacitors indicate that significant thermal losses are present in PPT–4. More than 50% of the terminal power is lost by conduction to the PPT walls in side–fed, 2–bar configurations at any capacitor energy. This trend is significantly lessened by running the PPT in capillary mode at higher capacitor energies. The best measured performance is in capillary mode at $E_o = 15$ J, in which case only 37% of the terminal power is lost as heat. Future 2–bar designs must pay particular attention to reducing the exposed insulator surface to reduce this heat loss.

At a standard operating stored capacitor energy E_o of 9 J, the average impulse bit for PPT–4 running in capillary mode is measured to be 29 ± 2 μN–s/J, corresponding to an I_{sp} of 745 ± 45 s, and a thruster efficiency η_t of $10.6 \pm 1.3\%$. Diodes in parallel with the discharge are used to prevent current reversal and improve efficiency. The impulse bit is broken down into its electrothermal and electromagnetic thrust components, resulting in $I_{ET}/E_o = 25$ μN–s/J and $I_{EM}/E_o = 4$ μN–s/J, so that electrothermal thrust contributes 86% of the total impulse while the remaining 14% is attributed to the electromagnetic process.

Transfer losses in the pulse–forming network are 11%. Conductive and radiative thermal losses ($\eta_h = 49\%$) in the thruster claim 51% of the terminal energy. Frozen flow ($\eta_f = 65\%$), divergence (η_{div} = 93%), and distribution (η_{dist} = 42%) losses in the exhaust consume the remaining lost energy.

The quadruple electrostatic probe measures a centerline electron density n_e at all tested energies ranging from $2.0 \pm 1.0 \cdot 10^{14}$ cm^{-3} to $1.0 \pm 0.5 \cdot 10^{13}$ cm^{-3}. Ascertaining a clear peak in centerline electron temperature is difficult due to system noise, but it is evident that at $E_o = 9$ and 15 J, T_e starts in the 2.0 ± 0.3 eV range and then cools off rapidly to 0.4 ± 0.06 eV. At $E_o =$ 5 J, T_e starts at 1.0 ± 0.2 eV and drops to 0.4 ± 0.06 eV.

The ion mach number u_i/c_m ranges from a supersonic 3.0 ± 0.5 to values exceeding 7.5 ± 1.1, corresponding to a hypersonic exhaust flow. By assuming thermal equilibrium ($T_e = T_i$) a maximum $c_m = 4.2$ km/s is calculated, corresponding to ion velocities ranging from 11 to 32 km/s, compared to the 34 km/s velocity calculated by measuring the arrival time of peak n_e.

Off–axis quadruple probe measurements indicate excellent symmetry in the plume with lower densities and higher temperatures compared to the centerline values.

A full nozzle and near–field plume survey with the B–probe indicates that the PPT–4 plume is not radially symmetric in B_θ. B_θ contour plots for constant 0°–180° and 90°–270° r–z planes are generated, and some mirrored symmetry is observed in the 90°–270° plane. The radial plume asymmetry corresponds to an radial electromagnetic thrust component, calculated to be only 4% of the overall PPT thrust. Additionally, the crossed electric and magnetic fields present in the plume result in a peak Hall parameter $\Omega = 0.4$ where the magnetic field is strongest, resulting in a modest decrease in plasma conductivity.

Acknowledgments

This work was partially funded by the Air Force Office of Scientific Research under contracts F49620–97–1–0138 and F49620–97–1–0443. Dr. M. Birkan is the program monitor. Additional support was provided by Naval Research Laboratory Grant No. N00173–98–P–0676 administered by M. Osborn of NRL and E. Pencil of NASA Glenn. We also thank Drs. R. Spores and G. Spanjers of the Air Force Research Laboratory who provided further support, resources, and counsel, and J. Frus of Unison Industries for his critical support in the development of the external circuit and the igniter system.

This work would not have been possible were it not for the machinists who built PPT–4 and its associated test equipment: S. Sprague, B. Johnson, K. Elam, D. Foley, D. Miller, and D. Tempel.

Additionally, we acknowledge the hard work and diligence of students E. Antonsen, F. Rysanek, M. Wilson, J. Norris, M. Morgan, T. Smart, T. Fritz, and J. Konicek.

<u>References</u>

1) Jahn, R. G., *Physics of Electric Propulsion,* McGraw–Hill Book Co., New York, NY, 1968.

2) Burton, R. L., and Turchi, P. J., "Pulsed Plasma Thruster," *Journal of Propulsion and Power*, Vol. 15, No. 5, 1998, pp. 716–735.

3) Akimov, V., Nagel, I., Ogloblina, I., Antropov, N., Pokryshkin, A., Popov, G., and Rudikov, A., "Analysis of PPT Potentialities in Solving the Satellite Orbit Control Tasks," *25th International Electric Propulsion Conference*, IEPC Paper 97–146, Aug. 1997.

4) Ebert, W. L., Kowal, S. J., and Sloan, R. F., "Operational Nova Spacecraft Teflon Pulsed Plasma Thruster System," *25th Joint Propulsion Conference*, AIAA Paper 89–2497, July 1989.

5) Meckel, N. J., Cassady, R. J., Osborne, R. D., Hoskins, W. A., and Myers, R. M., "Investigation of Pulsed Plasma Thrusters for Spacecraft Attitude Control," *25th International Electric Propulsion Conference*, IEPC Paper 97–128, Aug. 1997.

6) Blandino, J. J., Cassady, R. J., and Peterson, T. T., "Pulsed Plasma Thrusters for the New Millennium Interferometer (DS–3) Mission," *25th International Electric Propulsion Conference*, IEPC Paper 97–192, Aug. 1997.

7) Ziemer, J. K., Choueiri, E. Y., and Jahn, R. G., "Scaling Laws for Pulsed Electric Propulsion with Application to the Pluto Express Mission," *24th International Electric Propulsion Conference*, IEPC Paper 95–147, 1995.

8) Myers, R. M., Oleson, S. R., McGuire, M., Meckel, N. J., and Cassady, R. J., "Pulsed Plasma Thruster Technology for Small Satellite Missions," *9th AIAA/Utah State University Conference on Small Satellites*, NASA CR–1984271995, Sept. 1995.

9) Spanjers, G. G., Lotspeich, J. S., McFall, K. A., and Spores, R. A., "Propellant Losses Because of Particulate Emission in a Pulsed Plasma Thruster," *Journal of Propulsion and Power*, Vol. 14, No. 4, 1998, pp. 554–559.

10) Spanjers, G. G., and Spores, R. A., "PPT Research at AFRL: Material Probes to Measure the Magnetic Field Distribution in a Pulsed Plasma Thruster," *34th Joint Propulsion Conference*, AIAA Paper 98–3659, July 1998.

11) Turchi, P. J., Mikellides, I. G., Mikellides, P. G., and Schmahl, C. S., "Theoretical Investigation of Pulsed Plasma Thrusters," *34th Joint Propulsion Conference*, AIAA Paper 98–3807, July 1998.

12) Arrington, L. A., Haag, T. W., Pencil, E. J., and Meckel, N. J., "A Performance Comparison of Pulsed Plasma Thruster Electrode Configurations," *25th International Electric Propulsion Conference*, IEPC Paper 97–127, Aug. 1997.

13) Vondra. R. J., and Thomassen, K. I., "Performance Improvements in Solid Fuel Microthrusters," *Journal of Spacecraft and Rockets*, Vol. 9, No. 10, 1972, pp. 738–742.

14) Seeglitz, W. G., *A Study of a Cylindrical Pulsed Solid Fuel Microthruster*, M.S. Thesis, Massachusetts Institute of Technology, 1973.

15) Bushman, S. S., Burton, R. L., and Antonsen, E. L., "Arc Measurements and Performance Characteristics of a Coaxial Pulsed Plasma Thruster," *AIAA Joint Propulsion Conference*, AIAA Paper 98–3660, July 1998.

16) Wilson, M. J., Bushman, S. S., and Burton, R. L., "A Compact Thrust Stand for Pulsed Plasma Thrusters," *25th International Electric Propulsion Conference*, IEPC Paper 97–122, Aug. 1997.

17) Bushman, S. S., *Investigations of a Coaxial Pulsed Plasma Thruster*, M.S. Thesis. University of Illinois at Urbana–Champaign, 1999.

18) MicroSim, *PSpice Electric Circuit Simulator*, ver. 5.4, MicroSim, Irvine, CA, 1997.

19) Cassady, R. J., Meckel, N. J., Hoskins, W. A., Myers, R. M., Oleson, S. R., and McGuire, M., "Pulsed Plasma Thruster Systems for Spacecraft Attitude Control," *10th AIAA/Utah State University Conference on Small Satellites*, Sept. 1996.

20) SESAME, *The Los Alamos National Laboratory Equation of State Database, Teflon File 27190*. Los Alamos National Laboratory, LA–UR–92–3407, October, 1977.

21) Burton, R. L., and Bufton, S. A., "Exit–Plane Electrostatic Probe Measurements of a Low–Power Arcjet," *Journal of Propulsion and Power*, Vol. 12, No. 6, 1996, pp. 1099–1106.

22) Huddlestone, R. H., and Leonard, S. L. (ed.), *Plasma Diagnostic Techniques,* Academic Press, New York, 1965.

23) Burton, R. L., Delmedico, S. G., and Andrews, J. C., "Application of a Quadruple Probe Technique to MPD Thruster Plume Measurements," *Journal of Propulsion and Power*, Vol. 9, No. 5, 1993, pp. 771–777.

24) Chung, P. M., Talbot, L., and Touryan, K. J., *Electric Probes in Stationary and Flowing Plasmas,* Vol. 2, Springer–Verlag, New York, 1975.

25) Tilley, D. L., Kelly, A. J., and Jahn, R. G., "The Application of the Triple Probe Method to MPD Thruster Plumes," *21st International Electric Propulsion Conference*, AIAA Paper 90–2667, July 1990.

26) Burton, R. L., Wilson, M. J., and Bushman, S. S., "Energy Balance and Efficiency of the Pulsed Plasma Thruster," *34th Joint Propulsion Conference*, AIAA Paper 98–3808, July 1998.

27) Spitzer, L., *Physics of Fully Ionized Gases,* 2nd ed., Interscience Publishers, New York, 1962.

28) Sutton, G. P., *Rocket Propulsion Elements – An Introduction to the Engineering of Rockets,* 6th ed., John Wiley & Sons Inc., New York, NY, 1992.

29) Megli, T. W., Lu, J., Krier, H., and Burton, R. L., "Modeling Plasma Processes in 1–Kilowatt Hydrazine Arcjet Thrusters," *Journal of Propulsion and Power*, Vol. 14, No. 1, 1998, pp. 29–36.

Figures

Fig. 16: Off–axis n_e, E_o = 9 J, z = 1.3 cm, r = 2.1 cm.

Fig. 17: B–probe probing locations in the nozzle and plume of PPT–4. The 0°–180° plane is shown. The plug location corresponds to positive r. All locations are repeated in the 45°–225°, 90°–270°, and 135°–315° planes. The line at z = –24 corresponds to the deepest possible penetration into the thruster.

Fig. 18: B_θ signals for θ = 0°, 45°, 90°, 135°, 180°, 225°, 270°, and 315° at r = 8.1 mm (nozzle wall) and z = 24 mm. Minimum signal occurs at θ = 0°, where the spark plug is located. Peak signal occurs opposite the spark plug at θ = 180°.

Fig. 19: Contour plot of magnetic field strength B_θ at z = –24 mm and t = 2.5 μs (near peak current). Traces of constant enclosed current I_{enc} are designated as well as total current I_{tot} = 8.0 kA. The spark plug is at (x,y,z) = 15.7,0, –19.1 mm in the Cartesian system.

Fig. 20: Side–view contour plots of B_θ at t = 2.5 μs (near peak current). The spark plug is at (r,θ,z) = 15.7 mm, 0°, –19.1 mm. Positive values of r correspond to θ = 0° and θ = 90° on the respective plots.

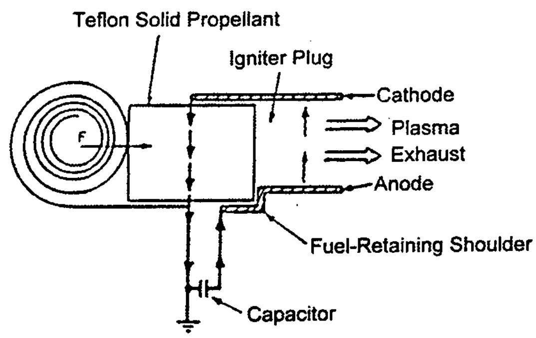

Fig. 1: Rectangular, breech–fed PPT from Vondra and Thomassen, 1972.

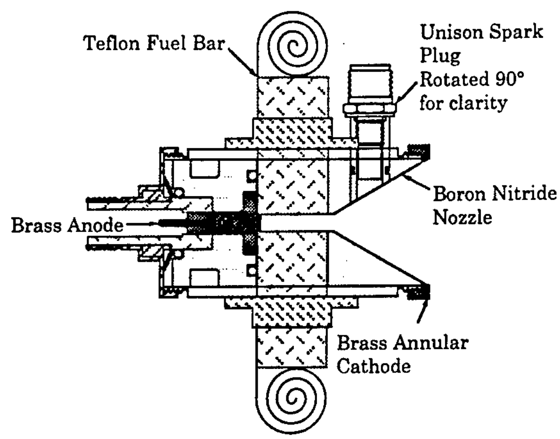

Fig. 2: Detailed schematic of PPT–4. In capillary mode side bars are replaced with a Teflon cylinder.

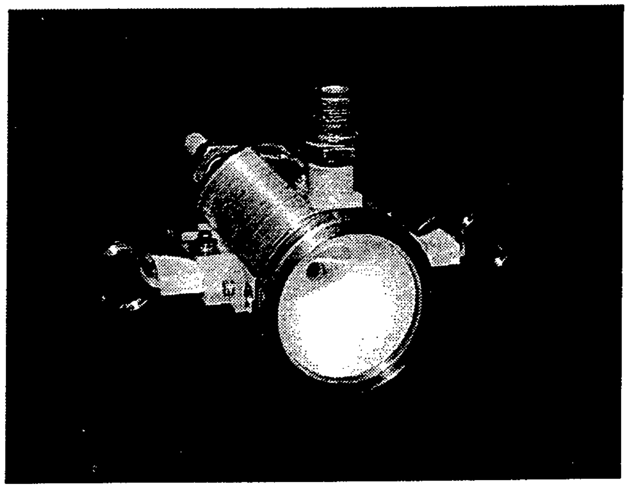

Fig. 3: PPT–4, Coaxial pulsed plasma thruster.

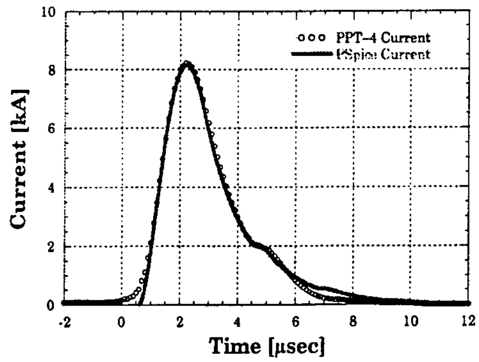

Fig. 4: PSpice matching of the PPT–4 current pulse at 9 J assuming constant impedances.

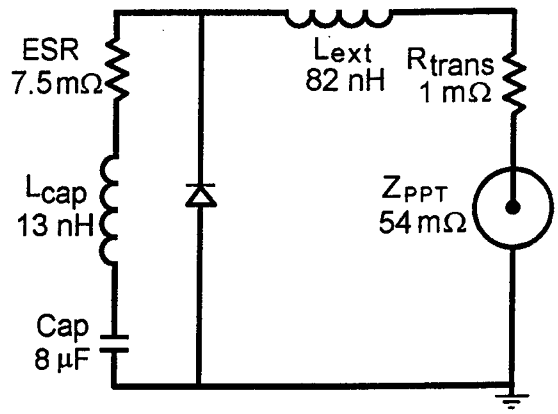

Fig. 5: PPT–4 circuit schematic from PSpice matching.

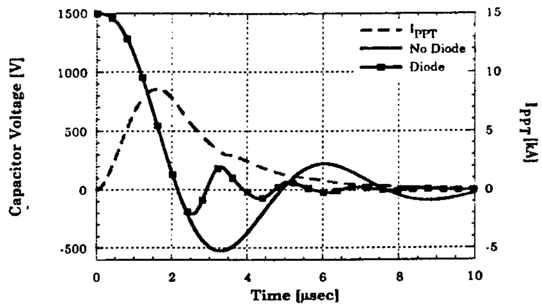

Fig. 6: Effect of diode on capacitor voltage reversal predicted by circuit modeling. The diode reduces voltage reversal from 33% to 13%.

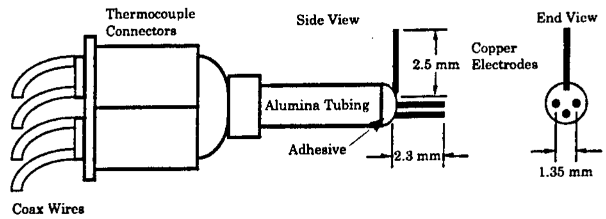

Fig. 7: Quadruple electrostatic probe schematic.

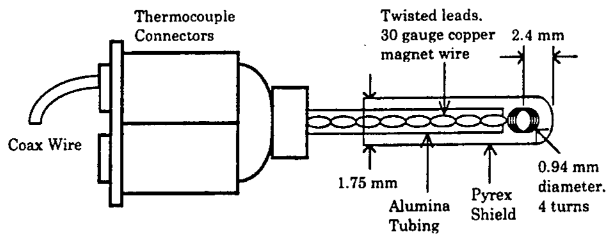

Fig. 8: Magnetic probe schematic.

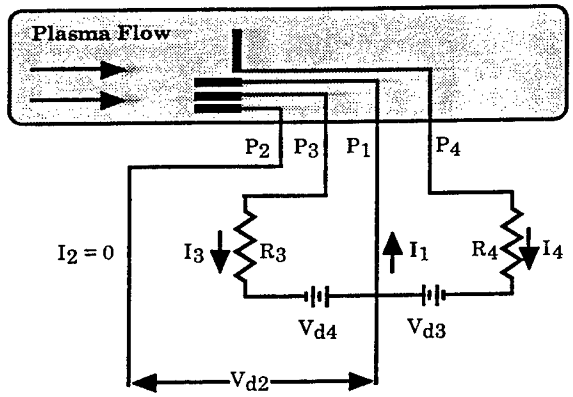

Fig. 9: Quadruple probe circuit schematic.

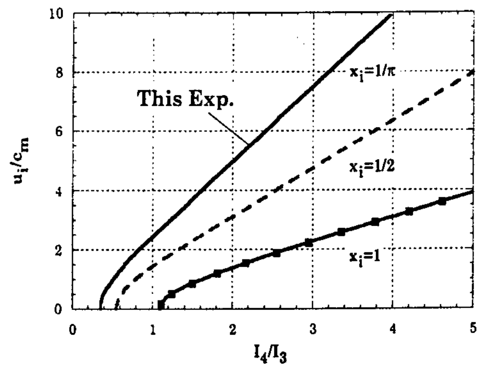

Fig. 10: Ion Mach number vs. crossed probe current ratio for different values of x_i, the geometric fraction of P_4 available for ion collection

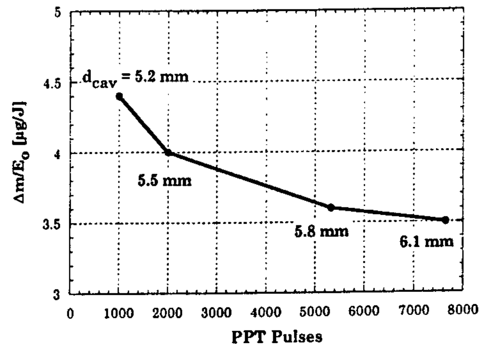

Fig. 11: Average mass loss per Joule versus shots fired. The "boring out" of the Teflon capillary results in a steadily increasing PPT cavity diameter which in turn ablates less mass.

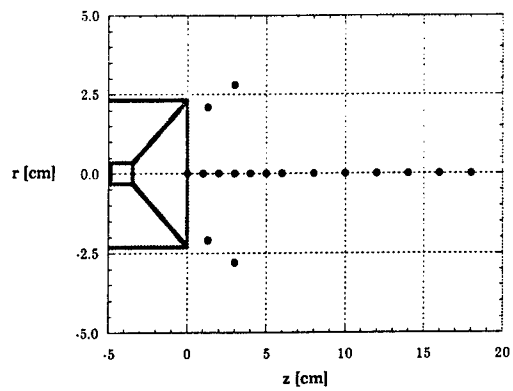

Fig. 12: Quadruple probe probing locations in the plume of PPT–4. The 0°–180° plane is shown; off–axis locations are repeated in the 90°–270° plane.

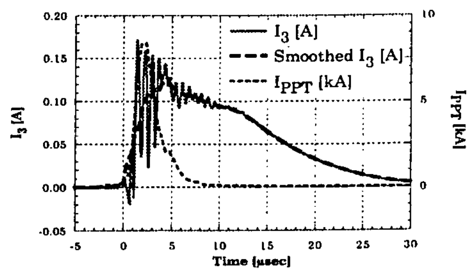

Fig. 13: Comparison of smoothed 10–shot–average data taken at $E_0 = 9$ J, $z = 1$ cm to raw 10–shot–averaged data. The large amount of noise before $t = 8$ μs renders that data unusable.

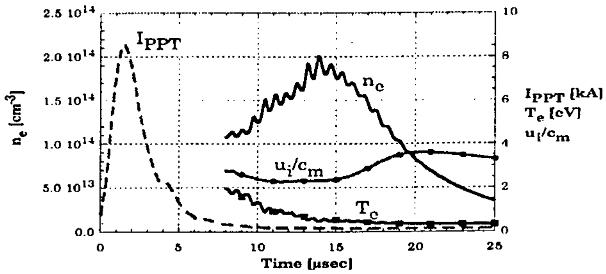

Fig. 14: Typical reduced centerline data from the quadruple probe. For this case, z = 3 cm and E_0 = 9J. While the magnitudes and peak times do vary, the shapes of the curves are relatively constant for all locations and energies.

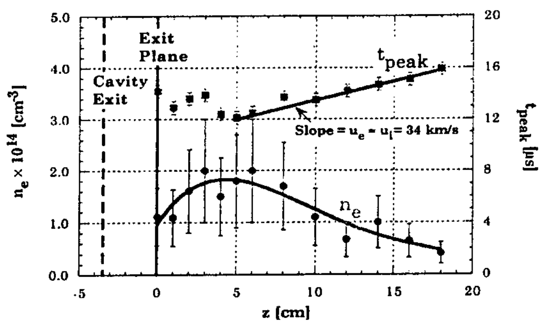

Fig. 15: Peak values of electron density and times of peak density versus distance from the exit plane at E_0 = 9 J. Curve fits illustrate electron/ion velocity and the shape of the electron density distribution.

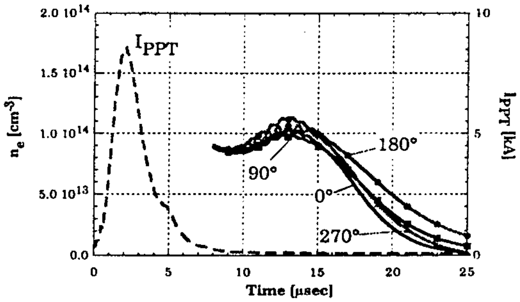

Fig. 16: Off–axis n_e, $E_o = 9$ J, z = 1.3 cm, r = 2.1 cm.

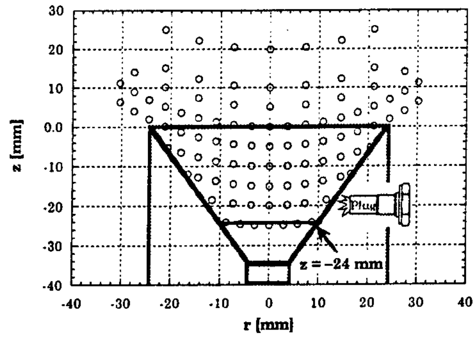

Fig. 17: B–probe probing locations in the nozzle and plume of PPT–4. The 0°–180° plane is shown. The plug location corresponds to positive r. All locations are repeated in the 45°–225°, 90°–270°, and 135°–315° planes. The line at z = –24 corresponds to the deepest possible penetration into the thruster.

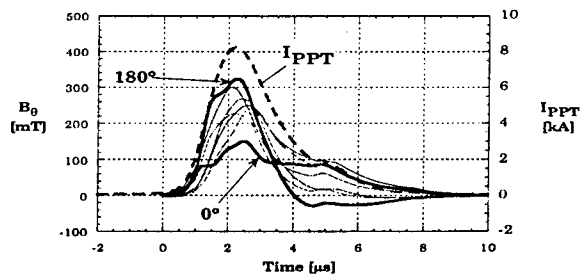

Fig. 18: B_θ signals for $\theta = 0°, 45°, 90°, 135°, 180°, 225°, 270°$, and $315°$ at $r = 8.1$ mm (nozzle wall) and $z = 24$ mm. Minimum signal occurs at $\theta = 0°$, where the spark plug is located. Peak signal occurs opposite the spark plug at $\theta = 180°$.

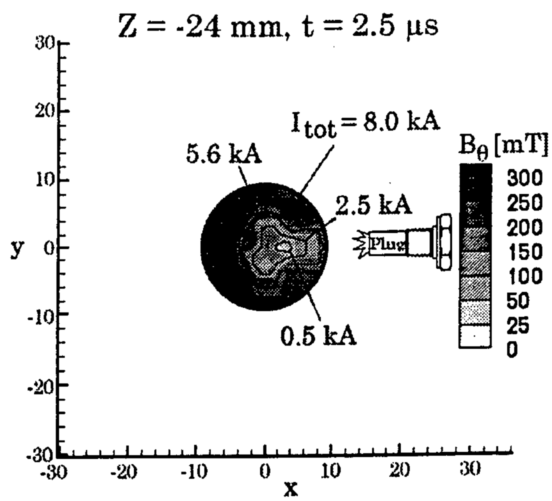

Fig. 19: Contour plot of magnetic field strength B_θ at $z = -24$ mm and $t = 2.5$ μs (near peak current). Traces of constant enclosed current I_{enc} are designated as well as total current $I_{tot} = 8.0$ kA. The spark plug is at (x,y,z) = 15.7,0, -−19.1 mm in the Cartesian system.

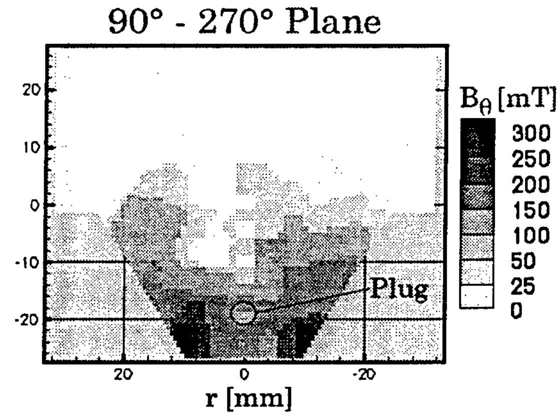

Fig. 20: Side–view contour plot of B_θ at t = 2.5 μs (near peak current). The spark plug, denoted by a circle, is at (r,θ,z) = 15.7 mm, 0°, –19.1 mm. Positive values of r correspond to θ = 90° on the plot.

Energy Measurements in a Coaxial Electromagnetic Pulsed Plasma Thruster

Erik Antonsen and Rodney L. Burton

ABSTRACT

An electromagnetic coaxial pulsed plasma thruster (PPT-5) with central igniter plug is investigated to understand the effects of diodes used to prevent current reversal in the arc and capacitor, and of propellant geometry and propellant material on energy losses and the ablation process. Teflon™ and high-density polyethylene propellant is axisymmetrically arranged around the central cathode in a fluted geometry. Thermocouple measurements and circuit modeling predict an arc impedance of 16 mΩ, a transfer efficiency of 89%, and thruster heating of 24%. The ablation is shown to depend strongly on the material type and the surface area in the z-θ plane facing the discharge. Scanning Electron Microscope analysis shows the presence of high carbon concentrations in the black areas on ablated Teflon, and also suggests internal sub-surface heating by the arc.

INTRODUCTION

This paper presents preliminary experiments on an electromagnetic coaxial pulsed plasma thruster (PPT-5), operating with Teflon™ and high-density polyethylene propellant. The difference between a "gasdynamic" and an "electromagnetic" PPT is illustrated by evaluating the electromagnetic thrust fraction f_{em}, defined in terms of the impulse $\int T dt$ as:

$$f_{em} = \frac{\int \frac{1}{2} L' I^2 dt}{\int T dt} = \frac{\int \frac{1}{2} L' I^2 dt}{\int \frac{1}{2} L' I^2 dt + \int T_{gasdyn} dt}$$

For an electromagnetic-type PPT, $\int \frac{1}{2} L' I^2 dt > \int T_{gasdyn} dt$. Expressions for L' for rectangular and coaxial PPTs are given in the Appendix and Ref. 1. For constant L', the current integral variable Ψ is introduced so that $\int \frac{1}{2} L' I^2 dt \equiv \frac{1}{2} L' \Psi$. The value of f_{em} for several PPTs[2-7] is given in Table 1. The Teflon MPD of Paccani is described in Ref. 8. The PPT-5 thruster is described further in this paper. Figure 1, based on Table 1 data, shows the correlation of f_{em} and specific impulse, with high f_{em} giving higher I_{sp}.

Thruster Design

The operational goals of the PPT-5 are:
1. Operate highly ionized, minimizing the neutral particle fraction.
2. Operate at the highest possible Ψ, maximizing jxB thrust.
3. Operate at high specific impulse, maximizing efficiency.

For high f_{em}, the usual tradeoff between I_{sp} and thrust does not pertain, since $1/2L'\Psi$ is not directly dependent on the ablated mass. Thus for an ideal electromagnetic PPT both the thrust and the thruster efficiency can be high to increase performance.

The electromagnetic thrust is estimated by assuming that the capacitor energy E_0 is completely discharged during a pulse, so that: $E_0 = \Psi Z_{tot}$, where Z_{tot} is the total ohmic and electromagnetic thrust impedance of the PPT circuit. The specific thrust is then:

specific thrust = $(1/2)L' / Z_{tot}$ [N-s/joule]

Table 1. Electromagnetic Thrust Fraction (f_{em}) for Teflon Pulsed Plasma Thrusters

Thruster	Type, feed	I_{sp}, s	Energy, J	L'[μH/m]	f_{em}
LES-6	rectangular, breech	312	1.85	0.92	0.24
LES-8/9, XPPT-1	rectangular, breech	1000	20	0.55	0.76
EO-1	rectangular, breech	*1350	50	0.67	0.50
MIPD-3	rectangular, side	1130	100	0.65	0.71
PPT-4	coax, side	850	9.0	0.66	0.16
PPT-5	coax, side	~2000	20	0.40	0.90
Teflon MPD	coax, side	1500	2000	0.44	~1.00

*based on breadboard unit

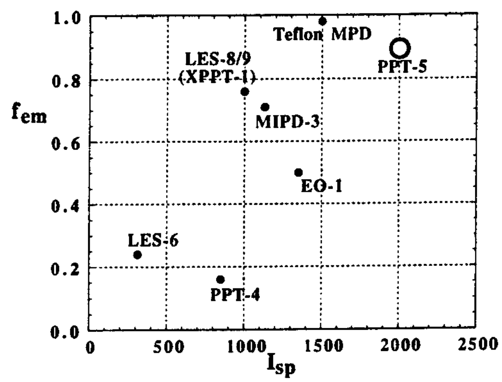

Fig. 1. EM thrust fraction vs. I_{sp}

The thruster efficiency is defined as:

$$\eta_t = \tfrac{1}{2}\left(\int T dt\right)\bar{u} / E_o,$$

where $\int T dt / E_o$ is the specific thrust. If the thrust is purely electromagnetic, $\int T dt = \frac{1}{2} L' \Psi$, so that

$$\eta_{t,em} = \tfrac{1}{4} L' \bar{u} / Z_{tot}$$

Operation in a mode where $\vec{j} \times \vec{B} >> \nabla p$ places a requirement on low Z_{tot} to increase specific thrust and efficiency. An indication of the lower limit of this impedance is given from experiments with a pulsed ablative-Teflon magnetoplasmadynamic (MPD) thruster for which the effective thruster impedance was measured as a function of energy and propellant type.[8] The lowest effective arc impedance was found to be Z_e = 8.6 mΩ for Teflon at the highest current tested, 11 kA.

This MPD result suggests that a Z_{tot} of 10 mΩ may be achievable for a PPT with a low-loss capacitor. As an example, L' = 0.66 μH/m would give a specific thrust of 33 μN-s/joule. Operation at an I_{sp} of 1500 s, also achieved by the same MPD thruster,[8] would give a thruster efficiency of 24%, and an I_{sp} of 5000 s would give an efficiency of 80%.

The contribution of electromagnetic acceleration of plasma to the impedance is derived from the electromagnetic thrust power and the mass-averaged velocity:

$$P_{em} = I^2 Z_{em} = \tfrac{1}{2}\left(\tfrac{1}{2} L' I^2\right)\bar{u}$$

which gives:

$$Z_{em} = \tfrac{1}{4} L' \bar{u}$$

The thruster efficiency is then $\eta_t = Z_{em} / Z_{tot}$. For the above example with L' = 0.66 µH/m and $I_{sp} = \bar{u} / g = 5000$ s, Z_{em} = 8 mΩ. Thus electromagnetic PPTs must inherently be low impedance devices. For Z_{tot} = 10 mΩ, only 20% of the energy is lost as ohmic heating.

It is well known that most pulsed plasma thrusters operate in the partially-ionized regime with a significant neutral fraction. As an indicator of the ionization fraction, the total charge transfer through the thruster arc is compared to the number of ablated atoms multiplied by the electronic charge. Define the ionization fraction parameter IFP as:

$$\mathrm{IFP} = \frac{\int |I| dt}{e N_{abl}}$$

The quantity eN_{abl} represents the charge transfer capability of the ablated mass if fully ionized. The use of the absolute value of the current inside the integral implies that each electron carries current only once and is then ejected from the thruster along with an ion, an assumption which does not hold if $\vec{j} \times \vec{B}$ is in the reverse thrust direction. The quantity IFP is shown for several PPTs in Table 2.

Table 2. Ionization Fraction Parameter (IFP) for Teflon PPTs

Thruster	I_{sp}, s	f_{em}	IFP
LES-6	312	0.24	0.09
LES-8/9(XPPT-1)	1000	0.76	0.56
EO-1	*1350	0.50	0.50
MIPD-3	1130	0.71	0.14
PPT-4	850	0.16	0.13
PPT-5	4000	0.90	0.3-1.3
Teflon MPD	1500	~1.00	0.91

*based on breadboard unit

Figure 2 shows IFP vs. f_{em} for a number of PPTs. The ionization fraction parameter generally increases with the electromagnetic thrust fraction.

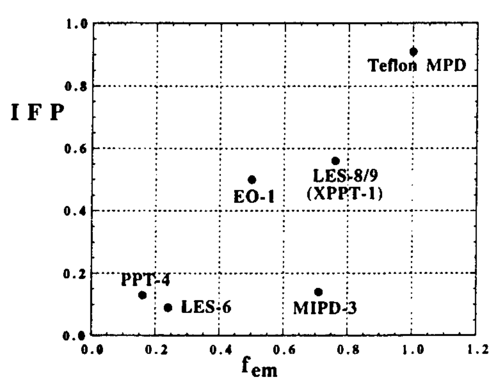

Fig. 2 Ionization fraction parameter for various PPTs

Table 2 suggests that many PPTs operate with a majority of neutrals, since more than enough charge carriers are available. It has been long recognized that this type of operation reduces thrust, as can be seen by comparing the example of the impulse from a bi-modal distribution of fast (m_f) and slow (m_s) particles.

$$m_f + m_s = m$$
$$\int T dt = m_f u_f + m_s u_s = m\bar{u}$$

$$KE = \frac{1}{2} m_f u_f^2 + \frac{1}{2} m_s u_s^2$$

It is often the case that $u_s << u_f$, in which case the energy and impulse of the slow particles is neglected, giving a ratio of thrust power to kinetic power:

$$\frac{\frac{1}{2}(m_f u_f + m_s u_s)\bar{u}}{KE} \approx \frac{m_f\left(m\bar{u}^2 / m_f\right)^{1/2}}{m\bar{u}} = \left(\frac{m_f}{m}\right)^{1/2}$$

This expression, a result of the assumed bimodal distribution in the particle velocities, is called the distribution efficiency, and represents a loss of thrust. In the limit $m_f = m$, no loss of thrust occurs, as for example with an ion thruster.

The goal with the present design is to operate with large IFP, in order to minimize the neutral fraction. The approach is to test a number of propellant configurations, measuring IFP for each type. A new thruster designated PPT-5 was designed for this study, with a central igniter plug, as shown in Figs. 3 and 4. The outer shell of the thruster is grounded and the central electrode (cathode) is pulsed at high voltage. Since the igniter plug is buried in the cathode, the plug exciter circuit is designed with high-voltage isolation (Fig. 5).

Fig. 3. PPT-5 Coaxial Pulsed Plasma Thruster

There are 4 possible diode configurations (Fig. 5) under which PPT-5 can operate: no diodes, diode electrically parallel to the arc, diode in series with the capacitor, or with both series and parallel diodes,. Normal PPT-5 operation uses diodes both in series and parallel, giving a current pulse shown in Fig. 6.

The effect of the parallel diode is to shunt the capacitor and its Equivalent Series Resistance (ESR), lowering capacitor heat loss and improving energy transfer to the discharge. The capacitor has an internal inductance, measured in a ring-down test to be ~30 nH. With only a parallel diode, this inductance produces a voltage and current reversal in the capacitor, which can be eliminated with the series diode. The resulting unipolar pulse increases capacitor life.

The thruster circuit was modeled using a constant arc impedance of 15 mΩ, and an ESR of the 34 µF Maxwell capacitor of 5 mΩ. The capacitor ESR was found by modeling of a NASA PPT circuit, in conjunction with a transfer efficiency measurement. Figure 7 shows the experimental arc current along with the model arc current, giving good agreement up to 20 µs, and capacitor voltage for the no-diode case. Figure 8 shows the experimental current along with the model arc current, capacitor voltage, and capacitor current for the parallel/series diode case. The figures show an increasing mismatch to the model late in the pulse, indicating higher impedance in the arc after approximately 20 µs. Figure 8 also shows a final voltage on the capacitor of 320 Volts, compared to experimental voltage measurements of 60 Volts.

Table 3 shows the distribution of energy loss in the PPT. In Case 1, with both series and parallel diodes, the Ψcap is only 50% of Ψ_{arc}. In Case 2, Ψ_{cap} is 75% of Ψ_{arc}. This reduced Ψ_{cap} is a result of the parallel diode, which shunts current away from the capacitor. The transfer efficiency for energy transferred from capacitor to arc shows a lower transfer efficiency for Case 2 because of current reversal in the capacitor. Case 3 has an even lower transfer efficiency because with no parallel diode $\Psi_{cap} = \Psi_{arc}$. Case 4, with no diodes, has the same transfer efficiency as Case 3 for the same reason.

Table 3. Calculated PPT-5 Circuit Losses

Case	Diodes	$\Psi=\int I^2dt$		η_{tr}
		Ψ_{cap}	Ψ_{arc}	
1	Series+Para	511	1028	0.86
2	Para	796	1057	0.80
3	Series	614	614	0.75
4	No Diode	1023	1023	0.75

Thermal Losses

Measurable thermal losses in PPT-5 include arc heating of the thruster, voltage sheaths, and capacitor heating. Capacitor heating is measured separately from other thermal transfer mechanisms, using Type K thermocouples placed at the base of the thruster head and near the terminals of the capacitor (Fig. 9).

The governing equation for heating is $\dot{Q} = (\Delta T/\Delta t)\Sigma mc_p$, where ΔT is the temperature rise, Δt is time, m is the sub-component mass and c_p is the specific heat. The thermal mass of the thruster head, Σmc_p, is calculated to be 622 J/°C with Teflon fuel and 590 J/°C with polyethylene. The thermal mass of the capacitor and the diode assembly is larger, 1250 J/°C.

The thruster head and capacitor are structurally and electrically connected by 12.7 mm aluminum rods and a copper inductor (not shown in Fig. 3), making it possible for heat to flow axially toward the capacitor, distorting the measurement. For the test setup, the axial heat flow is $\dot{Q} = \kappa A\Delta T/L$ where $kA/L = 0.17$ W/°C. Therefore the power loss measurements are most accurate at the beginning of the test where $\Delta T \sim 0$. Thermocouple data were taken at early times, eliminating the need for a heat flow correction.

Data are taken typically every 60 seconds during a 1000 pulse test at 20 Joules and 1.00 Hz. Figure 10 shows thermocouple data for a typical test using Teflon fuel. Table 4 gives the power lost through heating and the total power reaching the plasma. These tests were done both with and without diodes in the circuit. The cases with diodes showed higher heating in both the capacitor and the thruster head (Table 4). Total Heating at 20 W was 6.9 W with diodes and 9.0 W without diodes, an increase of 30%. Polyethylene shows about the same heating as Teflon. The Teflon measurements are in good agreement with the calculations of Table 3.

Mass Ablation

Several propellant geometries were tested at 20 J to determine the effect on mass ablation as shown in Table 5. The fuel configuration refers to the number of flutes and the percent of inner surface area in the z-θ plane. Figure 11 shows a frontal view of both 12/5 and 6/25 propellant configurations. The effect of increasing the number of flutes is an increase in the surface area of the sides of the flutes (r-z plane). In the 12/5 configuration the material comes to a peak less than half a millimeter across for a total of 5% surface in the z-θ plane. The material designations refer to the material of the fuel cup and the cathode ring, respectively. The cathode ring is a small disk of material that fills the gap between the inner surface of the fuel cup and the cathode outer diameter (Fig. 11).

The highest impedance values are associated with the minimum mass loss. The ionization fraction parameter varies from 0.32 to 1.30, implying a wide range in the ionization fraction.

The mass loss data was taken over 5000 pulses at 20 Joules and 1.0 Hz. Cases 4 and 5, with 25% surface area in the z-θ plane show higher ablation than cases 1 and 2 which have twice the surface area in the r-z plane. The total area in the z-θ plane exposed to the discharge is 0.71 cm^2 for the 12/5 configuration and is 3.38 cm^2 for the 6/25 configuration. For Teflon, the material of the cathode ring has a significant effect.

Table 4. PPT-5 Heat and Power Distribution

Location	Power at 20 J, 1.00 Hz		
	Teflon (diodes)	Teflon (no diodes)	Polyethylene (diodes)
Capacitor Power	20.0	20.0	20.0
Capacitor Heating	2.1	3.8	1.9
Thruster Heating	4.8	5.2	4.4
Net Power to Plasma	13.1	11.0	13.7

Table 5. Impedance Z_{tot} and ablated mass per pulse for various fuels and geometries at 20 J

Case	Fuel Config.	Z_{tot}, mΩ	μg/pulse	I F P
1	12/5 TFE/BN	25	30	0.62
2	12/5 TFE/TFE	24	15	1.28
3	12/5 HDPE/BN	45	2.5	1.30
4	6/25 TFE/BN	19	64	0.32
5	6/25 TFE/TFE	19	61	0.36
6	6/25 HDPE/BN	40	3.0	1.08

For cases 2 and 5 with a Teflon cathode ring, ablated mass per pulse decreased even though more Teflon was exposed to the arc. It therefore appears that the inward facing z-θ plane is the most significant factor for determining the total mass ablation. For all cases the cathode mass loss was 1.5-2.5 μg/pulse.

SEM Analysis

Scanning Electron Microscopy (SEM) was performed on as-machined and ablated Teflon and polyethylene fuel samples. The images at various magnifications (Figs. 12-25) show these surfaces at magnifications of 100x – 13000x. X-ray and back-scattered electron microanalysis was also used to determine the elemental makeup of selected Teflon samples. Teflon exhibited visual blackening in certain areas of the fuel after being ablated. Other Teflon areas were ablated leaving the original white color. Polyethylene did not exhibit distinct blackening but did show discoloration over the whole sample area exposed to the arc.

Figures 12 and 13 show both the as-machined Teflon and ablated Teflon at 250x magnification. The as-machined sample is featureless at 250x as was the case for all magnifications taken. The ablated images at 250x were in a region containing both cleanly ablated Teflon and blackened Teflon. The images show higher plateau-like areas that correspond to the blackened sections and lower smoother valleys corresponding to the white areas.

At 600x magnification (Figs. 14-15), the as-machined sample shows no features while the ablated sample shows the cleanly ablated areas to be full of bumps. The formation of similar bumps was serendipitously witnessed in real time on the SEM television monitor, and appeared to be bubbling caused by the SEM electron beam at magnifications greater than 13000x. The similarity of the electron beam-induced bubbling and the bumps observed at 600x without electron beam heating suggests that the heating is an internal bubbling process. However, as part of the SEM procedure a 3 nm thick gold layer is sputtered onto the samples and it is not clear what effect this may have on the bubbling behavior. At >13000x the bumps were observed to start as a bubble that opened to a fissure and collapsed. No pictures at magnifications greater than 13000x were taken due to this bubbling. If there is intensive sub-surface heating during PPT operation, this phenomenon may also suggest a mechanism for late-time ablation observed by Spanjers.

At 13000x magnification, three images were taken to show the difference between the blackened areas and the white areas. Figure 16 shows the relatively featureless reference sample of as-machined Teflon. The second image (Fig. 17) was taken in a white area of the ablated fuel and shows both smooth dark areas and small white nodules of 0.4 μm diameter. Figure 18 was taken in a blackened area of the ablated fuel showing much rougher texture with white nodules also present.

The white nodules on the ablated fuel may be deposited brass from the cathode. The SEM electron backscattering diagnostic showed that the nodules had a higher average atomic number and were not a topographical feature. X-ray microanalysis, which has a 1 μm lateral resolution and penetrates to a depth of 2.5 μm, was conducted and traces of copper were found to be present in the nodule. Copper was also found in the regions adjacent to the nodules, possibly due to nodules buried in the Teflon material, or due to the 1 μm lateral resolution. The x-ray analysis penetrates to 2.5 μm and could measure unseen nodules. Figure 19 shows the results of this scan for the 3 areas depicted in Figs. 16-18.

From the x-ray analysis the amount of carbon in the blackened areas is noticeably higher than in either of the other two cases (Fig 19). This leads to the conclusion that the blackened areas contain carbon ash.

One limitation of the x-ray diagnostic is that it favors lighter elements and some weak lines of heavier elements. Many of the heavier elements have their strongest lines above 10 kV, an energy which overheats the Teflon samples, making it difficult to go to higher energies required to see heavier elements. While weak gold and copper lines showed up, any evidence of a weak iron line from the steel igniter plug was saturated by the fluorine line and is unknown at this time. The same may hold true for the zinc component of the brass cathode. There was also an oxygen peak of unknown origin noted for the case of the blackened Teflon analysis.

Similar images (Figs. 20-25) were taken of polyethylene but no analysis was performed for elemental composition. The as-machined sample for polyethylene is shown in Fig. 20 at 600x magnification. Higher magnification did not show more detail and resulted in burning of the sample. As with Teflon, the as-machined surface is fairly featureless.

The ablated polyethylene shows much different characteristics from both the as-machined sample and ablated Teflon. Figure 21 shows a 100x magnification image of the ablated polyethylene with a pattern different from the Teflon case. The surface shows a grain structure, possibly due to a material grain or the machining process. Focusing on the peaks at 250x and 1000x magnification shows a layered, flaking detail (Figs. 22-23). Further magnification to 13000x on a peak and in a valley is depicted in Figs. 24 and 25. There is evidence that the discharge removes polyethylene from the valleys and leaves the peaks behind, ablating them at a slower rate.

CONCLUSIONS

An electromagnetic coaxial PPT (PPT-5) is operated with two propellant materials and varying propellant geometries to achieve low neutral fraction, high specific impulse, and high specific thrust. For Teflon, experimental data suggests that mass ablation can be controlled by varying the amount of propellant surface area in the z-θ plane. Propellant surface area in the r-z plane had less impact on measured mass ablation. Locating propellant at the cathode decreased the mass ablated per pulse. The Teflon mass loss was an order of magnitude higher than that of the polyethylene, so that the polyethylene is generally more highly ionized.

The PPT-5 requires a low impedance external pulse circuit to operate at high **jxB** thrust. A discharge impedance of 16 mΩ was achieved at 20 J by using series and parallel diodes in the external circuit to provide pulse shaping, with a capacitor having an ESR of 5 mΩ. Still lower impedances are desirable to raise the electromagnetic thrust component.

Thermocouple heating data and current modeling show that the parallel and series diodes have a favorable effect on the transfer efficiency of the thruster. The series diode prevents current and voltage oscillations in the capacitor, and the parallel diode shunts the capacitor after the first current peak, reducing heating by a factor of two. The capacitor heating is 10%, and the thruster heating is 24% of the stored energy.

SEM analysis suggests that Teflon and polyethylene have different ablation mechanisms. The highest magnifications for both fuels show different features. Images of ablated Teflon show surface features that suggest internal bubbling, possibly caused by a sub-surface heating mechanism, as yet unexplained. X-ray analysis of ablated Teflon shows a significant increase in carbon in the blackened areas, suggesting the presence of Teflon ash. The polyethylene images show regions with flaking interspersed with relatively undisturbed surfaces, but do not suggest a reason for the vastly different ablation rates of the two materials.

ACKNOWLEDGEMENTS

We are indebted to G. Paccani of The University of Rome "La Sapienza," and W. Deininger of Ball Aerospace for illuminating discussions on pulsed thruster operation. We would like to thank: F. Rysanek of UIUC for aid with the SEM measurements, K. Elam and D. Foley of the Department of Theoretical and Applied Mechanics machine shop for expert fabrication of the thruster, N. Meckel of Primex Aerospace Corporation for sharing data relating to the EO-1 pulsed plasma thruster, E. Pencil of NASA Glenn for the loan of experimental equipment enabling us to perform this investigation, and J. Frus of Unison Industries for his critical support in the development of the external circuit and the igniter system. The SEM analysis was carried out by V. Petrova in the Center for Microanalysis of Materials, University of Illinois, which is supported by the U.S. Department of Energy under Grant DEFG02-ER-45439. This work was funded by the Air Force Office of Scientific Research, under Grant No. F49620-97-1-0138. M. Birkan is the Program Monitor.

REFERENCES

1. Burton, R. L. and Turchi, P. J., "Pulsed Plasma Thruster," *J. Propulsion and Power*, Vol. 14, No. 5, pp. 716-735, Sept.-Oct. 1998.
2. Solbes, A. and Vondra, R. J., "Performance Study of a Solid Fuel-Pulsed Electric Microthruster," *J. Spacecraft and Rockets*, Vol. 10, No. 6, pp. 406-410, Nov.-Sept. 1973.
3. Vondra, R., Thomassen, K., and Solbes, A., "A Pulsed Electric Thruster for Satellite Control," *Proceedings of the IEEE*, Vol. 59, No. 2, 1971, pp. 271-277.
4. Spanjers, G. G., McFall, K. A., Gulczinski, F. S., III, and Spores, R. A., "Investigation of Propellant Inefficiencies in a Pulsed Plasma Thruster," AIAA paper 96-2723, July 1996.
5. Arrington, L. A., Haag, T. W., Pencil, E. J., and Meckel, N. J., "A Performance Comparison of Pulsed Plasma Thruster Electrode Configurations," 25th International Electric Propulsion Conf., IEPC paper 97-127, Aug. 1997.
6. Antropov, N. N., Krivosonov, I. G., Popov, G. A., and Rudikov, A. I., "PPT Model Experimental Refinement," AIAA paper 96-2728, July 1996.
7. Burton, R. L., and Bushman, S. S., "Probe Measurements in a Coaxial Gasdynamic PPT," AIAA paper 99-2288, June 1999.
8. Paccani, G., Chiarotti, U., and Deininger, W. D., "Quasisteady Ablative Magnetoplasmadynamic Thruster Performance with Different Propellants," *Journal of Propulsion and Power*, Vol. 14, No. 2, Mar-Apr 1998, pp. 254-260.
9. Guman, W. J. and Peko, P. E., "Solid-Propellant Pulsed Plasma Microthruster Studies," *Journal of Spacecraft and Rockets*, Vol. 6, No. 6, 1968, pp. 732-733.
10. Kerrisk, J. F., "Current Distribution and Inductance Calculations for Rail-Gun Conductors," Los Alamos National Lab, LA-9092-MS, Los Alamos, NM, 1981.
11. Anderson, H. L. (ed.), *Physics Vade Mecum*, American Institute of Physics, New York, 1981.
12. Jahn, R. G., "Physics of Electric Propulsion," McGraw-Hill Book Company, New York, 1968.

APPENDIX:

Inductance Gradient Formulas

The electromagnetic impulse bit can be calculated from $(1/2)L'\Psi$ if the current-squared integral is measured and the inductance gradient L' is known.[1] Since the current distribution in the circuit conductors of a PPT does not in general satisfy the conditions of uniformity assumed by available inductance formulas, a potential-theory solution based in part on the distributions of resistivity and ion velocity in the plasma is then required. The inductance formulas here assume fixed current-density distributions and must be used with caution. Under the usual mode of PPT operation the plasma discharge remains adjacent to the ablating surface of the propellant, and if the current distribution within the plasma does not change with time, the electromagnetic impulse can be estimated from $(1/2)L'\Psi$ using the formulas.

The inductance of a closed circuit of rectangular conductors of length ℓ[11] is:

$$L = 0.4\left[\frac{3}{2}\ell + \ell\left(\frac{d}{b+c}\right) - d + 0.22(b+c)\right] [\mu H] \quad (A1)$$

so that:

$$L' = 0.6 + 0.4 \ln\left(\frac{d}{b+c}\right) \text{ [}\mu\text{H/m]} \qquad \text{(A2)}$$

where d is the electrode separation, and each electrode has width b and thickness c.

For coaxial thrusters the inductance gradient is readily calculated if the current density is axisymmetric. For thrusters with an annular electrode of radius r_a and a central electrode of radius r_c, the inductance gradient L' is determined by assuming azimuthal current symmetry and uniform axial current density to the central electrode. For this case L' is identical to that calculated for the magnetoplasmadynamic thruster:[12]

$$L'[\mu H/m] = \frac{\mu_o}{2\pi}\left(\ln\frac{r_a}{r_c} + \frac{3}{4}\right) \qquad \text{(A3)}$$

For more complex geometries, e. g. flared or diverging rectangular electrodes, L' must be calculated from the vector potential method used by Kerrisk,[10] or from IL' = ϕ', where the flux gradient ϕ' is determined at the plane of symmetry from magnetic probe measurements.